# *A Lagrangian perspective on the Atlantic and Pacific precipitation-evaporation asymmetry*

JGR Atmospheres

RESEARCH ARTICLE
10.1029/2023JD039087

# A Lagrangian Perspective on the Atlantic and Pacific Precipitation-Evaporation Asymmetry

**P. M. Craig[1], D. Ferreira[1], and J. Methven[1]**

[1]Department of Meteorology, University of Reading, Reading, UK

**Key Points:**

- Airmass trajectories used to partition atmospheric moisture fluxes across catchment boundaries into ocean basins that water originates from
- Moisture fluxes crossing catchment boundaries have little contribution from remote ocean basins and are dominated by the two adjacent basins
- Atmospheric moisture import to the Pacific drainage basin is dominated by trajectories with Indian Ocean origin rather than Atlantic origin

**Correspondence to:**
P. M. Craig,
philip.craig@reading.ac.uk

**Citation:**
Craig, P. M., Ferreira, D., & Methven, J. (2023). A Lagrangian perspective on the Atlantic and Pacific precipitation-evaporation asymmetry. *Journal of Geophysical Research: Atmospheres*, *128*, e2023JD039087. https://doi.org/10.1029/2023JD039087

Received 17 APR 2023
Accepted 28 NOV 2023

**Author Contributions:**
**Conceptualization:** P. M. Craig, D. Ferreira, J. Methven
**Formal analysis:** P. M. Craig
**Funding acquisition:** D. Ferreira, J. Methven
**Methodology:** P. M. Craig, D. Ferreira, J. Methven
**Supervision:** D. Ferreira, J. Methven
**Validation:** P. M. Craig
**Visualization:** P. M. Craig
**Writing – original draft:** P. M. Craig, D. Ferreira, J. Methven
**Writing – review & editing:** P. M. Craig, D. Ferreira, J. Methven



**Abstract** Total precipitation minus evaporation ($P - E$) for the Atlantic is negative while it is approximately neutral for the Pacific. This has frequently been attributed to westward Atlantic-to-Pacific moisture flux across Central America. However, this Eulerian perspective has limited scope as it does not consider the origins of the water crossing ocean drainage basin boundaries and the possibility that it has remote sources. By using an airmass trajectory model, we take a Lagrangian approach to investigate the origin of the moisture contributing to fluxes, $Q_n$, across these boundaries. $Q_n$ is partitioned into contributions from each basin, the stratosphere and trajectories not assigned an origin. The total $Q_n$ across each basin boundary are mainly composed of contributions from the two adjacent basins while remote or stratospheric origins make small contributions. Partitioning $Q_n$ shows that the atmosphere exports ∼1 Sv water vapor from the Atlantic, Indian and Pacific basins with a similar quantity imported to the Pacific. However, Atlantic and Indian atmospheric imports are ∼0.5–0.6 Sv. Normalizing by drainage basin perimeters reveals that the import to these basins is half as efficient as Pacific import. Partitioning $P - E$ into contributions from other basins shows that Pacific moisture import is dominated by trajectories with Indian basin origin (∼38%, or 0.43 Sv, of total Pacific import). The import is greatest in boreal summer due to the Asian monsoon flow and stronger westward flux across Central America. These anomalies dominate the difference in annual imports between the Pacific, Atlantic and Indian basins.

**Plain Language Summary** Precipitation and evaporation are approximately balanced across the Pacific Ocean drainage basin while the Atlantic and Indian basins have surpluses of evaporation. This has previously been explained by strong westward atmospheric moisture transport from the Atlantic across Central America to the Pacific in the trade winds. However, this hypothesis does not account for moisture that is transported from remote sources. We have used an airmass trajectory model to calculate pathways of moisture for 14 days prior to arrival at the ocean drainage basin catchment boundaries and determine the origins of moisture crossing the boundaries then partition the cross-boundary moisture flux into contributions from each ocean basin. We find that most of the cross-boundary flux is explained by contributions from the two basins directly adjacent to the boundaries and remote sources are negligible in comparison. Partitioning the moisture fluxes also shows that the Atlantic, Indian and Pacific basins export similar quantities of moisture but the atmosphere imports less moisture to the Atlantic and Indian basins. Moisture with origin from the Indian basin makes up 38% of the moisture imported to the Pacific. This mainly occurs in boreal summer and shows the role of the Asian Summer Monsoon.

## 1. Introduction

Atmospheric moisture transport between ocean basins plays an important role in maintaining the contrasting atmospheric moisture budgets (precipitation minus evaporation; $P - E$) between the Atlantic, Pacific and Indian Oceans. The Pacific has an approximately neutral budget ($P - E \approx 0$) while the other two show strong net evaporation (Craig et al., 2017, 2020). These characteristics have been linked to the asymmetries in sea surface salinity (SSS) and meridional overturning circulations (MOC). Briefly, the larger net evaporation over the Atlantic drives higher SSS in that basin than in the Pacific, notably at high latitudes. The higher SSS, hence denser surface waters, favor deep water formation in the subpolar North Atlantic as part of the Atlantic MOC. There is no analog in the subpolar North Pacific where there are comparatively fresher and lighter surface waters (Broecker, 1991; Ferreira et al., 2010, 2018).

Previous studies have assessed the link between inter-basin atmospheric moisture fluxes and the $\overline{P - E}$ (overbar denotes time mean) asymmetries from an Eulerian perspective. Notably, many studies have focused on

Atlantic-to-Pacific water vapor flux across Central America, sometimes more specifically on the Isthmus of Panama, as a key ingredient of the large $\overline{P-E}$ contrast between the Atlantic and Pacific (Broecker, 1991; Leduc et al., 2007; Lohmann, 2003; Schmittner et al., 2011; Sinha et al., 2012; Wang et al., 2013; Zaucker & Broecker, 1992). Craig et al. (2020), however, showed that atmospheric moisture flux across Central America is close to the zonal mean zonal moisture flux: in that sense, it is not anomalous and cannot contribute to the zonal asymmetry between the Atlantic and Pacific. Instead, it is the westward Indian-to-Pacific moisture flux over South-East Asia associated with the Asian Summer Monsoon that deviates substantially from the zonal mean and causes anomalous moisture transport into the Pacific basin, resulting in strong area-averaged precipitation (Craig et al., 2017) and neutral $\overline{P-E}$.

The Eulerian approach to understanding the $\overline{P-E}$ asymmetries does not account for the origin of moisture. Arguments focusing on moisture transport across Central America assume (either explicitly or implicitly) that moisture evaporated from the Atlantic is transported across Central America in the easterly trade winds and falls as precipitation across the Pacific. While this may be largely true, the possibility for long range atmospheric moisture transport from the Indian or Southern Oceans is not discussed, and neither is moisture which evaporated from the Pacific and advected all the way back to its source basin via the global circulation. Furthermore, such arguments focus on the time-mean perspective with the easterly trade winds crossing Central America and westerly advection at mid-latitudes. Craig et al. (2020) (Supporting Information) showed that, while the monthly mean flow dominates low latitude atmospheric moisture flux, there are also substantial contributions from sub-monthly fluxes to the climatological atmospheric moisture budgets of each ocean drainage basin in the mid- to high latitudes. These sub-monthly fluxes are associated with complex pathways, such as recirculation across boundaries and westerly fluxes above Central America.

Most notably, the sub-monthly fluxes contribute a net export from the Pacific, a negative contribution to $\overline{P-E}$ ($-0.46$ Sv, 1 Sv $\equiv 10^9$ kg s$^{-1}$), almost counteracting the positive $\overline{P-E}$ contribution from the monthly mean flow. Craig et al. (2020) also highlighted the importance of the seasonal cycle in the $\overline{P-E}$ asymmetries by showing that the contrast in budgets between the basins is greatest in the northern hemisphere summer when the Atlantic and Indian basins reach their peak negative $\overline{P-E}$ and the Pacific basin reaches peak positive $\overline{P-E}$. The Lagrangian approach introduced here takes other key mechanisms of atmospheric moisture transport into account (e.g., transient fluxes associated with large-scale weather systems, monsoon systems (Baker et al., 2015) and low-level jets (LLJs; Marengo et al., 2004; Nicholson, 2016; Whyte et al., 2008)) that may influence the $\overline{P-E}$ asymmetries, and also long range transport between remote ocean basins that are not directly adjacent to catchment boundaries.

There are only three previous studies that specifically address the $\overline{P-E}$ ocean basin asymmetries using Lagrangian techniques. Stohl and James (2005), using 10 days forward trajectories from each ocean basin, concluded that air from the North Pacific produces negative $\overline{P-E}$ over the North Atlantic and that air from the Indian Ocean "produces" positive $\overline{P-E}$ over the Pacific. Singh et al. (2016) used numerical water tracers to investigate how the moisture budget and salinity asymmetry amplify with global warming; they find that, with warmer temperatures, enhanced Atlantic-to-Pacific atmospheric moisture transport is due to greater distances between the source and sink regions and that moisture residence time increases. Using a Lagrangian trajectory model that traces atmospheric water mass flux, Dey and Döös (2020) found that atmospheric moisture transport in the midlatitude westerlies across "Afro-Eurasia" contributes 0.4 Sv to midlatitude Pacific precipitation compared to 0.26 Sv from the easterly trade winds. However, Dey and Döös (2020) did not discuss the role of the Indian Ocean and the Asian Summer Monsoon highlighted in other studies (Craig et al., 2020; Czaja, 2009; Emile-Geay et al., 2003; Ferreira et al., 2018).

There are several studies that have used Lagrangian methods to trace precipitation origins on a global scale (Dey et al., 2023; Gimeno et al., 2010; van der Ent & Savenije, 2013). Despite using very different methods, these global studies show that most of the Atlantic Ocean provides moisture for continental precipitation. However, van der Ent and Savenije (2013) found that only narrow regions of the eastern Pacific Ocean provide significant moisture for continental precipitation (>250 mm year$^{-1}$ ocean evaporation is transported to the continent), whereas Gimeno et al. (2010) identified both northern and southern Pacific subtropical highs as major source regions.

Overall, this suggests that much of the evaporated moisture rains out before reaching land due to the width of the basin. The relative widths of the Atlantic and Pacific basins was suggested as a contributing factor (Ferreira

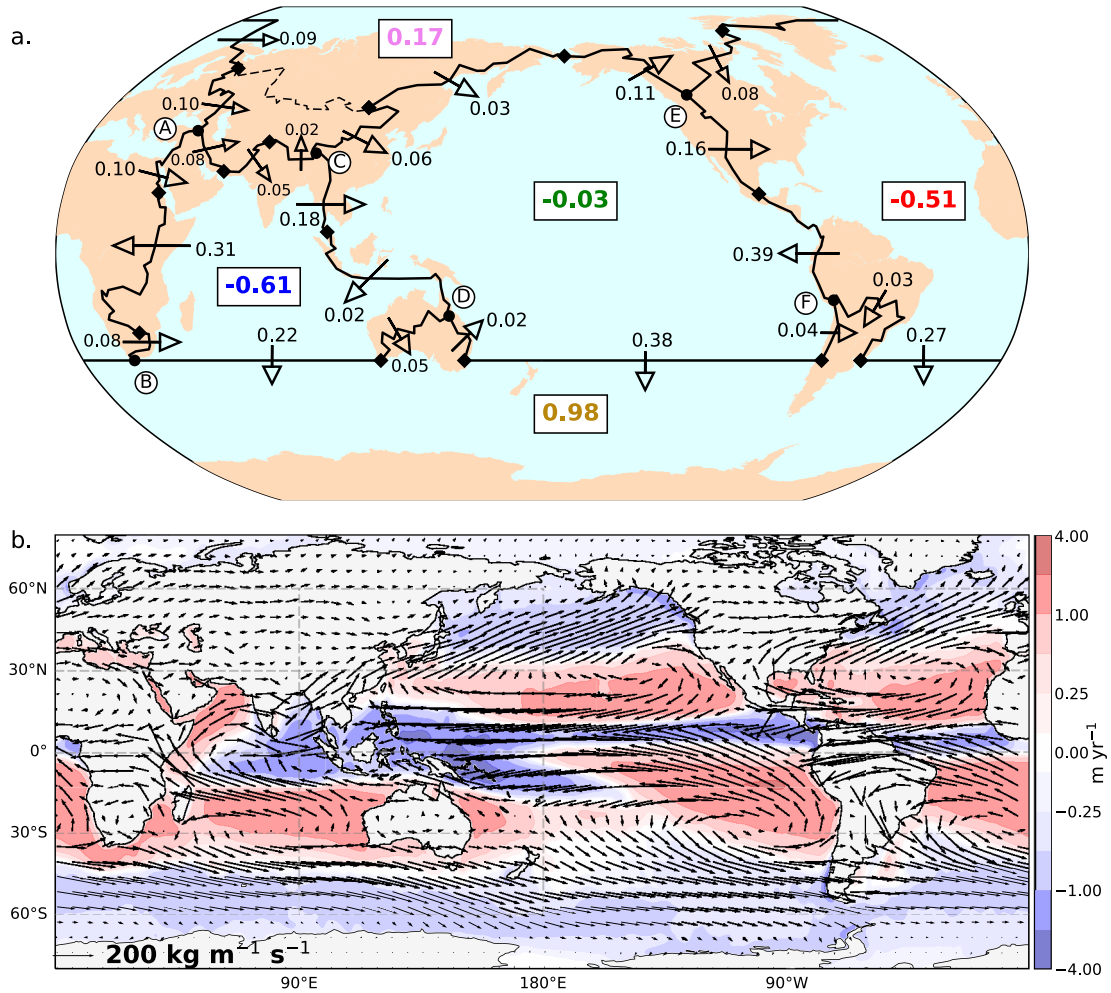


**Figure 1.** (a) Annual mean (2010–2014) ERA-Interim vertically and horizontally integrated moisture fluxes ($Q_n$) normal to the catchment boundaries (solid black lines) in Sv. The values in boxes show $\overline{P-E}$ are the sum of the surrounding $Q_n$ in Sv using Equation 3. The black circles (labeled A, B, C, D, E, and F) indicate the nodes of the Arctic and Southern Ocean catchment boundaries where they meet the American, African and South-East Asian catchment boundaries and the black diamonds show where the catchment boundaries are split into segments based on either geographical reasons or the change in net direction of $Q_n$. The dashed black line in panel (a) is the northern boundary of the Central Asian endorheic basin. (b) Vertically integrated moisture fluxes in kg $m^{-1}$ $s^{-1}$ (see bottom left for scale). The color shading indicates the annual mean vertically integrated moisture flux divergence from Equation 2 (in m $year^{-1}$).

et al., 2010; Schmitt et al., 1989; Wills & Schneider, 2015), with the greater width of the Pacific basin resulting in low levels of moisture export by the atmosphere—a point to be addressed in this study.

Here, we aim to improve the understanding of the moisture transport between ocean drainage basins, specifically addressing the following questions:

1. Does the moisture flux crossing the catchment boundaries have origin in neighboring basins or are there substantial remote sources?
2. How can the $\overline{P-E}$ asymmetry between ocean basins be understood using the trajectories?
3. What are the key dynamical processes affecting the $\overline{P-E}$ asymmetry?

To address these questions, we propose a different approach to previous studies. Rather than attempting to directly link precipitation distributions over each ocean drainage basin to moisture origins, we release back trajectories from the catchment boundaries of the ocean drainage basins (Figure 1a) to find the origins of the water contributing to the moisture flux (Sections 2.3 and 2.4). This approach permits the separation of the total moisture fluxes into entering and leaving contributions as well as the partition of the flux into contributions from each drainage basin. The effect of these contributions on basin-wide precipitation and the atmospheric moisture budget is then inferred through conservation of moisture (see Section 2.2). With this approach we can establish whether the

anomalous water vapor flux crossing the Southeast Asia catchment boundary into the Pacific basin during the Asian Summer Monsoon (Craig et al., 2020) mostly originates in the Indian Ocean basin or has some substantial contribution from remote ocean basins.

## 2. Methods

A Lagrangian approach was taken to partition the fluxes of atmospheric moisture across catchment boundaries into contributions of water from different origin basins using re-analysis wind data to calculate air mass back trajectories and to determine specific humidity along those paths. The data used in this study are described in Section 2.1, followed by the moisture budget equations in Section 2.2 with the trajectory model and calculations described in Section 2.3. The criteria for assigning moisture origins are defined in Section 2.4 and the trajectory integration time is justified in Section 2.5. The calculation for kernel density estimation are presented in Section 2.6.

### 2.1. Data

We use six-hourly data from the ECMWF Reanalysis - Interim (ERA-Interim) reanalysis from the European Center for Medium Range Weather Forecasts (ECMWF) for the years 2010–2014 (Dee et al., 2011). We have used only 5 years since the interannual variability of basin-scale $P - E$ is relatively small (Craig et al., 2017) and the required of number of trajectories per year (~20.3 million per year) constrains the scale of the calculation. ERA-Interim uses a 4D-VAR data assimilation scheme with 12-hourly analysis cycles which combine observations with prior information from the model. The spectral data are output by the ECMWF forecast model (Integrated Forecasting System) and transformed onto a reduced N128 Gaussian grid and 60 hybrid $\eta$ model levels (Simmons & Burridge, 1981).

### 2.2. Moisture Budget Calculations

The vertical integral of moisture flux normal to catchment boundaries surrounding the ocean drainage basins is calculated at points along the boundaries by the following integral:

$$Q_n = \frac{1}{g}\int_0^1 \overline{q\mathbf{v}} \cdot \hat{\mathbf{n}} \frac{\partial p}{\partial \eta} d\eta, \tag{1}$$

where $\hat{\mathbf{n}}$ is the unit vector normal to the boundary, $\mathbf{v}$ is the horizontal wind vector, $q$ is specific humidity, $\eta$ is the ERA-Interim vertical co-ordinate, $p$ is pressure, $g$ is acceleration due to gravity and the overbar denotes a time mean. The integral of $Q_n$ along a catchment boundary between any two points $X$ and $Y$ (Figure 1a) is expressed as $Q_{XY}$.

The atmospheric moisture budget at a point is obtained from the vertical integral of the mass continuity equation for water vapor (Berrisford et al., 2011; Craig et al., 2017):

$$\frac{1}{g}\int_0^1 \nabla \cdot \overline{q\mathbf{v}} \frac{\partial p}{\partial \eta} d\eta = E - P, \tag{2}$$

where the storage term for total column water vapor has been omitted since it is orders of magnitude smaller than the divergence term on long time scales (Craig et al., 2017; Trenberth et al., 2011). Using the Divergence Theorem on Equation 2 for an ocean drainage basin, the domain-integrated $E - P$ can be related to the fluxes through the drainage boundary:

$$E - P = \frac{1}{g}\oiint_{\partial V} \overline{q\mathbf{v}} \cdot \hat{\mathbf{n}} \frac{\partial p}{\partial \eta} d\eta\, dl = \sum_{XY} Q_{XY}, \tag{3}$$

where $\partial V$ is the boundary of the drainage basin and $dl$ is the elemental length along the boundary. By convention, $\hat{\mathbf{n}}$ is inward pointing and a moisture flux entering a drainage basin is counted positive. In the last equality of Equation 3, the sum is calculated on the all $XY$ segments surrounding a drainage basin. The power of Equation 3

is that any decomposition of $Q_{XY}$ using the Lagrangian approach (e.g., origin, entering/leaving) can be projected onto contribution to the basin scale $P - E$.

### 2.3. Trajectory Model

The Reading Offline Trajectory (ROTRAJ) model (de Leeuw et al., 2017; Methven, 1997; Methven et al., 2001) is used to calculate back trajectories from the catchment boundaries surrounding the five ocean drainage basins (Craig, 2019). ROTRAJ calculates trajectories offline by integrating the trajectory equation,

$$\frac{D\mathbf{x}}{Dt} = \mathbf{u}(\mathbf{x}, t), \tag{4}$$

with a fourth order, four stage Runge-Kutta method (Press et al., 2003) using ERA-Interim spectral data on the full Gaussian grid.

Atmospheric variables required for the diagnostics are interpolated to the trajectory location at 6 hr time step using bilinear interpolation in the horizontal direction, cubic vertical interpolation and linear time interpolation (Methven, 1997). These are specific humidity $q$, potential vorticity (PV), pressure $p$, boundary layer (BL) height $z_{\mathrm{BL}}$ and temperature $T$, zonal wind $u$, meridional wind $v$ and surface pressure $p_{\mathrm{surf}}$.

### 2.4. Defining Moisture Origins

We follow de Leeuw et al. (2017) to define the moisture origin of an air mass trajectory by the location of last increase in water vapor mixing ratio through rapid vertical mixing connected with the surface beneath. The rationale is that in a well-mixed BL, or capping cloud layer, the turbulent mixing is rapid within the column and therefore the mixing ratio is reset, irrespective of the prior history of the air parcel. After this event, specific humidity is close to conserved, since mixing is weak above the BL, unless saturation and condensation occurs when the specific humidity must decrease. de Leeuw et al. (2017) define two origin categories (CAT I, II) differing in the type of mixing layer experienced.

CAT I origins occur when a trajectory last exits the turbulent BL. The ERA-Interim BL height ($z_{\mathrm{BL}}$) is defined using the Bulk Richardson number $\left(R_{i_{b(z)}}\right)$ where $z_{\mathrm{BL}}$ is the first level above the surface where $R_{i_{b(z)}} > 0.25$ (ECMWF, 2015). This definition of $z_{\mathrm{BL}}$ only defines the dry BL height, which is approximately the same as the cloud base height (von Engeln & Teixeira, 2013), so latent heat release is not accounted for. In unsaturated conditions the virtual potential temperature ($\theta_v$) is well-mixed (Emmanuel, 1994) so air properties at the trajectory origin location are closely related to $\theta_v$, temperature and humidity at the ocean surface beneath. de Leeuw et al. (2017) present evidence on the link between moisture origin and the surface properties, as well as the tight relationship between last exit from the BL and the maximum specific humidity along the trajectory. CAT I origins are only assigned when a trajectory exits the BL above the ocean (as determined by the ERA-Interim land-sea mask) in order to link moisture fluxes to oceanic moisture origins (Figure 2, blue dashed line). Therefore, if a trajectory crosses the coast inside the BL it is assigned CAT I origin at the coast.

Trajectories which do not pass below $z_{\mathrm{BL}}$ may still experience mixing within the cloud layer above the dry BL (Figure 2, green dashed line). A trajectory is assigned CAT II origin if the equivalent potential temperature, $\theta_e$ (Bolton, 1980), increases by at least 2.5 K over three consecutive 6 hr time steps with an accompanying increase in $q$ to exclude dry mixing (de Leeuw et al., 2017). Since $\theta_e$ is well mixed in a moist BL, it is assumed that $\theta_e$ diagnosed at the origin location is approximately equal to $\theta_e$ at the surface below. CAT II origins are permitted to occur over land if the criterion is satisfied, as any regions with high convective activity and moisture recycling are included (e.g., Amazon and Congo rainforests).

Trajectories which are released in the stratosphere or which have recently been in the stratosphere before arrival (Figure 2) are assigned stratospheric origin. These trajectories are dry and do not contribute significantly to $Q_n$. A trajectory is diagnosed as being in the stratosphere if it is above the dynamical tropopause, that is, $\theta > 350$ K or PV > 3 potential vorticity units (PVU; 1 PVU $\equiv 10^{-6}$ K m$^2$ kg$^{-1}$ s$^{-1}$). Trajectories which fulfilled either of these criteria were also checked to ensure their height above the surface exceeded 6 km to exclude low trajectories with high PV in the BL or at high latitudes.

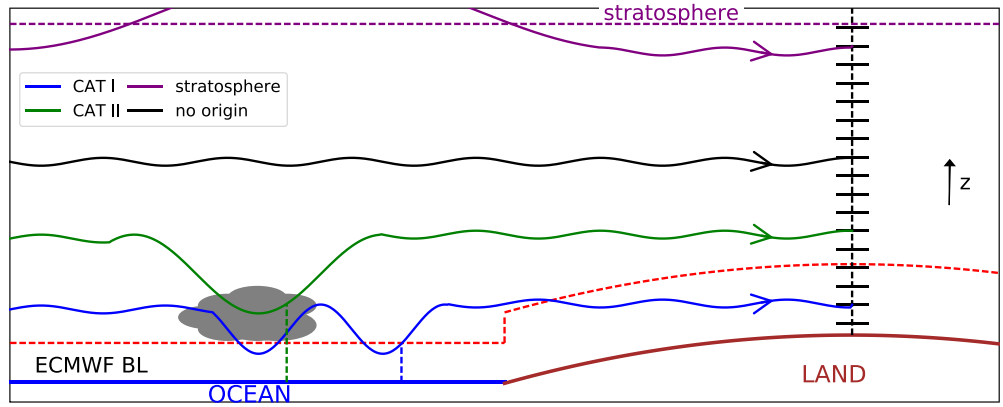


**Figure 2.** Schematic showing the different trajectory origin categories: boundary layer (BL) origin (CAT I, blue), cloud layer mixing (CAT II, green), stratosphere (purple) and no origin (black). The trajectory with CAT I origin is assigned origin upon its last exit from the ocean BL (at location of dashed blue line). In this example the trajectory enters the BL above the land after exiting the ocean BL before arriving at the catchment boundary (black dashed line). The trajectory with CAT II origin experiences mixing in a cloud (dashed green line) above the top of the ECMWF BL (dashed red line) where $\theta_e$ and $q$ both increase. The trajectory with stratospheric origin exits the stratosphere (bounded by the tropopause, dashed purple line) before arriving at the catchment boundary. The solid black lines at the catchment boundary are the $\eta$ levels on which back trajectories are initialized.

Trajectories that cannot be assigned one of CAT I, CAT II or stratospheric origins within the trajectory integration time (Section 2.5) are categorized as having no origin (Figure 2). All trajectories with or without origin are used to calculate $Q_n$ using $q$ and $\mathbf{v}$ at the trajectory initialization time:

$$Q_n = \frac{1}{g}\int_0^1 q_{t=0}\mathbf{v}_{t=0}\cdot\hat{\mathbf{n}}\frac{\partial p}{\partial \eta}\,\mathrm{d}\eta\,\mathrm{d}l. \tag{5}$$

### 2.5. Trajectory Integration Time

While still a highly debated topic in the literature, estimates of the average residence time of water in the atmosphere range between 4 and 10 days (Läderach & Sodemann, 2016; Trenberth, 1998; van der Ent & Tuinenburg, 2017). Based on these, previous Lagrangian studies have typically used 10-day long trajectories, a time required to identify sources of moisture for precipitation. In the present study, we focus instead on atmospheric moisture fluxes crossing the catchment boundaries of ocean drainage basins to partition it into contributions associated with origin in the different ocean drainage basins.

To determine the optimal integration time for our purpose, we conduct a test experiment with 30-day back trajectories from the American catchment boundary (Figure 1). Back trajectories are released from points along the catchment boundaries approximately 75 km apart (Craig, 2019) on 17 evenly spaced $\eta$ levels (from 0.95 to 0.15) every 12 hr at 00 and 12 UTC over July 2010. Data are then output in pressure co-ordinates.

The proportion of trajectories which can be assigned an origin monotonically increases with the trajectory length (Figure 3a). Initially, more trajectories have CAT II origin than CAT I but as the trajectory length increases beyond 8 days the number of trajectories with CAT II origins decreases. This is because CAT II origins are reassigned to CAT I origins as trajectories make contact with the BL above the ocean and CAT I origins are prioritized over CAT II origins (Section 2.4). Close inspection of Figure 3a reveals small fluctuations on the total, CAT I and CAT II lines. These are caused by the diurnal cycle of BL height which peaks in daytime so more trajectories can make contact with the BL. The fluctuations disappear with increasing integration time as the trajectories are spread out across different longitudes and therefore less susceptible to the diurnal cycle of BL height.

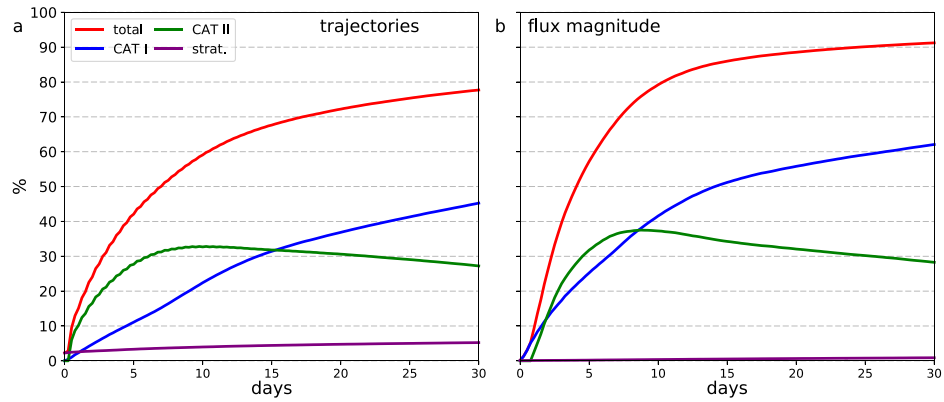


**Figure 3.** Evolution of (a) proportion of trajectories and (b) flux magnitude from trajectories with all origin types (red), CAT I origins (blue), CAT II origins (green) and stratospheric origins (purple) as trajectory length is increased. These results are averaged over trajectories released every 12 hr from the American catchment boundary (Figure 1) in July 2010. The sum of the CAT I, CAT II and stratosphere lines is equal to the red lines in both panels.

We also compute the magnitude of the moisture flux explained by trajectories as a function of the integration time:

$$Q_n^L = \frac{1}{g} \oiint_{\partial V} q_{t=0} |\mathbf{v} \cdot \hat{\mathbf{n}}| \frac{\partial p}{\partial \eta} \, \mathrm{d}\eta \, \mathrm{d}l \tag{6}$$

where $q_{t=0}$ is specific humidity for each trajectory at the time the trajectory is initialized (i.e., at the time it crosses the catchment boundary). The Lagrangian flux $Q_n^L$ is then compared to the Eulerian flux $Q_{XY}$. Results are shown in Figure 3 as a percentage. The contribution to the moisture flux from trajectories with CAT I and II origins largely dominates while the contribution from trajectories with stratospheric origin is very weak (less than 1%) as these trajectories have very low $q$. Results in other months and on other catchment boundaries are broadly similar.

Based on these results, 14-day back trajectories were considered to be sufficient for the purposes of this study due to the proportion of $|Q_n|$ (typically 85%) explained at this length. This is a compromise also based on the storage space limitations and available memory for the trajectory calculations. Back trajectories are released from the catchment boundaries surrounding each ocean drainage basin (Figure 1) throughout 2010–2014. The annual mean atmospheric moisture budgets and the asymmetries between the Pacific and Atlantic/Indian Oceans over this time period (Figure 1) are similar to the longer 36-year ERA-Interim climatology (Craig et al., 2020, their Figure 1) with differences of less than 0.1 Sv in all basins. This is in line with findings of Craig et al. (2017) who showed that the interannual variability of basin-scale $P - E$ is small. While our analysis period is limited to 2010–2014, we expect it has little quantitative impact on the basin-scale budgets of interest here, and on our conclusions. Overall, there are 101,508,135 trajectories. A sample data set of the trajectories has been made available at the University of Reading's Research Data Archive (Craig, 2023).

### 2.6. Kernel Averaging

Finally, to understand the trajectory origins, the density of origins, $\rho(\mathbf{x})$, can be calculated using a smooth kernel function, $K_i(\mathbf{x})$, at all locations, $\mathbf{x}$, within a 200 km radius of the trajectory origin $\mathbf{x}_i$:

$$\rho(\mathbf{x}) = \frac{1}{n} \sum_{i=1}^{n} K_i(\mathbf{x}) \tag{7}$$

where $n$ is the number of trajectories (Hodges, 1996; Silverman, 1986) and $\rho(\mathbf{x})$ has units of trajectories steradian$^{-1}$ month$^{-1}$ (steradian is the unit a solid angle). This method is not sensitive to the map projection and gives a smoother field than a 2D histogram (Methven et al., 2001).

To understand how the trajectory origin density fields relate to $Q_n$, the density fields from Equation 7, $\rho(\mathbf{x})$, are weighted by the flux density contribution from each trajectory $F_i = (1/g) q \mathbf{v} \cdot \hat{\mathbf{n}} \, \mathrm{d}p \, \mathrm{d}l$, where $\mathrm{d}p$ is the pressure

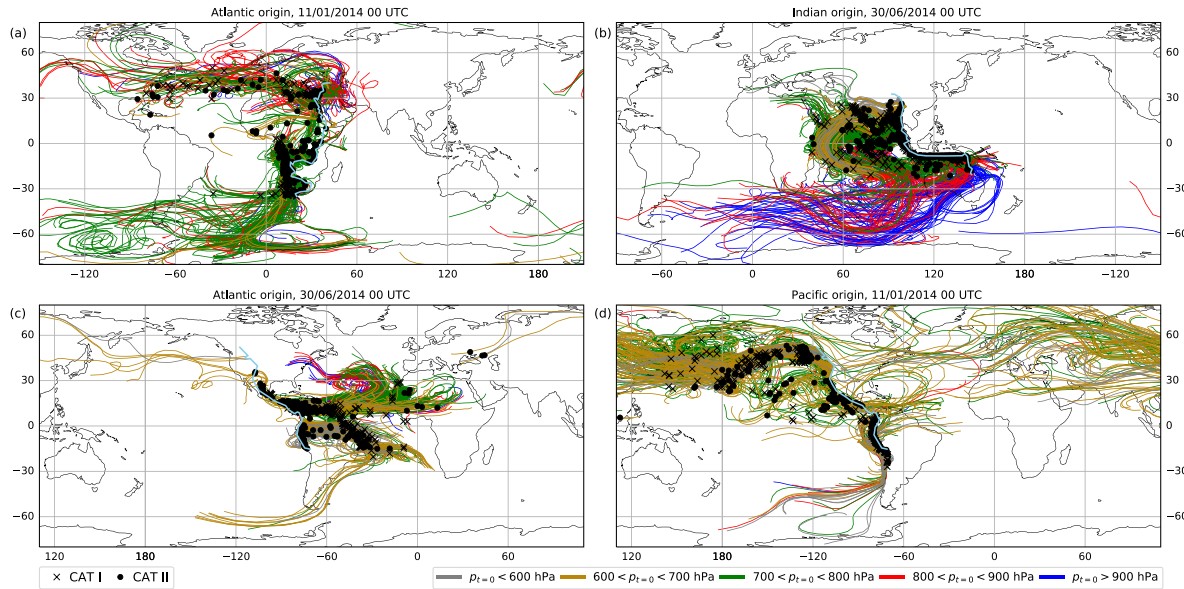


**Figure 4.** Trajectories released from (a) the African catchment boundary at 00 UTC on 11 January 2014 with Atlantic origin, (b) the South-East Asian catchment boundary at 00 UTC on 30 June 2014 with Indian Origin, (c) the American catchment boundary at 00 UTC 30 June 2014 with Atlantic origin and (d) the American catchment boundary at 00 UTC on 11 January 2014 with Pacific origin. Trajectories are colored by their pressure at release from the catchment boundary ($p_{t=0}$) and the entire 14-day paths of the trajectories are shown even when their origins are much closer to the catchment boundaries. CAT I (crosses) and CAT II (circles) origin locations are also shown. The catchment boundaries are shown in light blue.

difference between $\eta$-levels and d$l$ is the distance between points along a catchment boundary, to relate the contribution to humidity flux across a catchment to a map of origin locations:

$$Q_n(\mathbf{x}) = \sum_{i=1}^{n} F_i \, K_i(\mathbf{x}). \tag{8}$$

## 3. Density of Trajectory Origins

The trajectory origins of four trajectory release case studies (Figure 4) show that most trajectories have CAT I origin on or close to the catchment boundaries from which they were released. Many CAT I origins are also found along the coasts of the continent their catchment boundary lies on when $z_{\mathrm{BL}}$ is low during the night (Figure 4a). Many CAT I origins can also found further away from the catchment boundaries if their trajectories are released at higher altitudes with the air transported in the northern hemisphere storm tracks above 600 hPa (Figures 4a and 4d). CAT II origins can be found in regions where mixing and convection occur such as the storm tracks at low latitudes. In regions where $z_{\mathrm{BL}}$ is very high and there are high levels of convective activity, such as the Maritime Continent, most origins (of both types) appear to occur along the catchment boundary (Figure 4b).

### 3.1. Number Density

Origin densities are greatest close to, or in the vicinity of, the catchment boundaries where the density often exceeds 150 trajectories steradian$^{-1}$ month$^{-1}$ (Figure 5). This is particularly the case where the boundary crosses open ocean or is near the coast (e.g., South-East Asia) since CAT I origins are permitted if a trajectory is released inside the BL above the ocean (Figure 2). There are clear coastal maxima in some locations for trajectories released from specific catchment boundaries: along the South American Atlantic coast for the Americas and Southern Atlantic boundary, the East African coast for the African boundary, Canada's Pacific coast for the Arctic Atlantic and Pacific boundaries, the Middle East and South Asian coasts for the Arctic Indian boundary, and the East Australian coast for the Southern Indian and Pacific boundaries. This is a result of coastal outflow where the BL height is greater above land than above the ocean (Dacre et al., 2007; Peake et al., 2014).

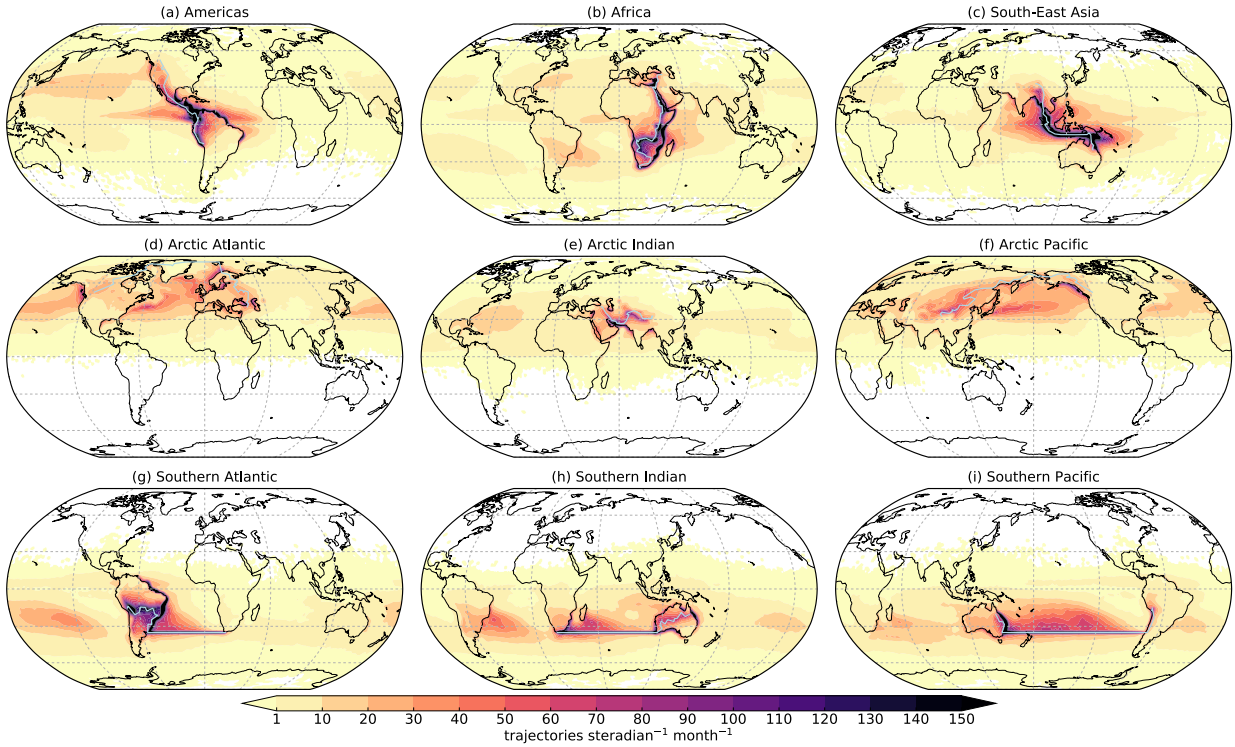


**Figure 5.** Annual mean (2010–2014) density maps of all origins of trajectories released from each catchment boundary (shown in light blue on each map). Units are trajectories steradian$^{-1}$ month$^{-1}$.

Neighboring basins dominate the proportions of trajectories with an assigned origin from each catchment boundary (Table 1). Although trajectories with no assigned origin in 14 days have the greatest proportion in all but one catchment boundary (Arctic Atlantic), they contribute little to $Q_n$ (Figure 3b). When they are discounted, the trajectories with origin in the two neighboring basins generally account for the majority of the remaining trajectories. For example, trajectories with origin in the Atlantic and Pacific basins account for 57.8% of the total trajectories released from the American catchment boundary (88.8% when discounting the trajectories with no origins).

Each sector of the Arctic catchment boundary has a substantially greater proportion of trajectories with stratospheric origin, with nearly one quarter of trajectories released from the Atlantic sector having stratospheric origin. This is because lower altitude of the tropopause at these latitudes combined to its downward sloping which

**Table 1**
*Proportions of Trajectories as Percentages (Rounded to One Decimal Place) Released From Each Catchment Boundary With Origin in the Atlantic, Indian, Pacific, Arctic and Southern Drainage Basins, Stratosphere or Without Origin in 14 Days*

| Boundary (XY) | $n$ (×10$^3$) | Atlantic | Indian | Pacific | Arctic | Southern | Stratosphere | None |
|---|---|---|---|---|---|---|---|---|
| Americas (EF) | 9,626 | 29.6 | 0.6 | 28.2 | 0.4 | 0.2 | 6.1 | 34.9 |
| Africa (AB) | 13,290 | 21.0 | 23.1 | 3.1 | 0.3 | 2.1 | 2.8 | 47.7 |
| South-East Asia (CD) | 10,247 | 1.5 | 29.6 | 32.6 | 0.4 | 0.6 | 1.1 | 34.2 |
| Arctic Atlantic (EA) | 12,234 | 28.1 | 0.5 | 12.1 | 7.8 | 0.0 | 24.6 | 26.9 |
| Arctic Indian (AC) | 6,396 | 16.0 | 15.7 | 3.6 | 6.6 | 0.0 | 12.8 | 45.3 |
| Arctic Pacific (CE) | 13,662 | 9.7 | 2.2 | 22.7 | 11.5 | 0.0 | 23.0 | 30.8 |
| Southern Atlantic (FB) | 11,449 | 26.7 | 0.9 | 12.2 | 0.0 | 16.4 | 0.8 | 42.9 |
| Southern Indian (BD) | 11,427 | 7.9 | 20.5 | 7.0 | 0.0 | 18.0 | 1.2 | 45.4 |
| Southern Pacific (DF) | 13,165 | 2.9 | 6.4 | 27.5 | 0.0 | 17.6 | 1.6 | 44.1 |

*Note*. The number of trajectories $n$ for each catchment boundary is shown in the second column. All percentages are rounded to one decimal place.

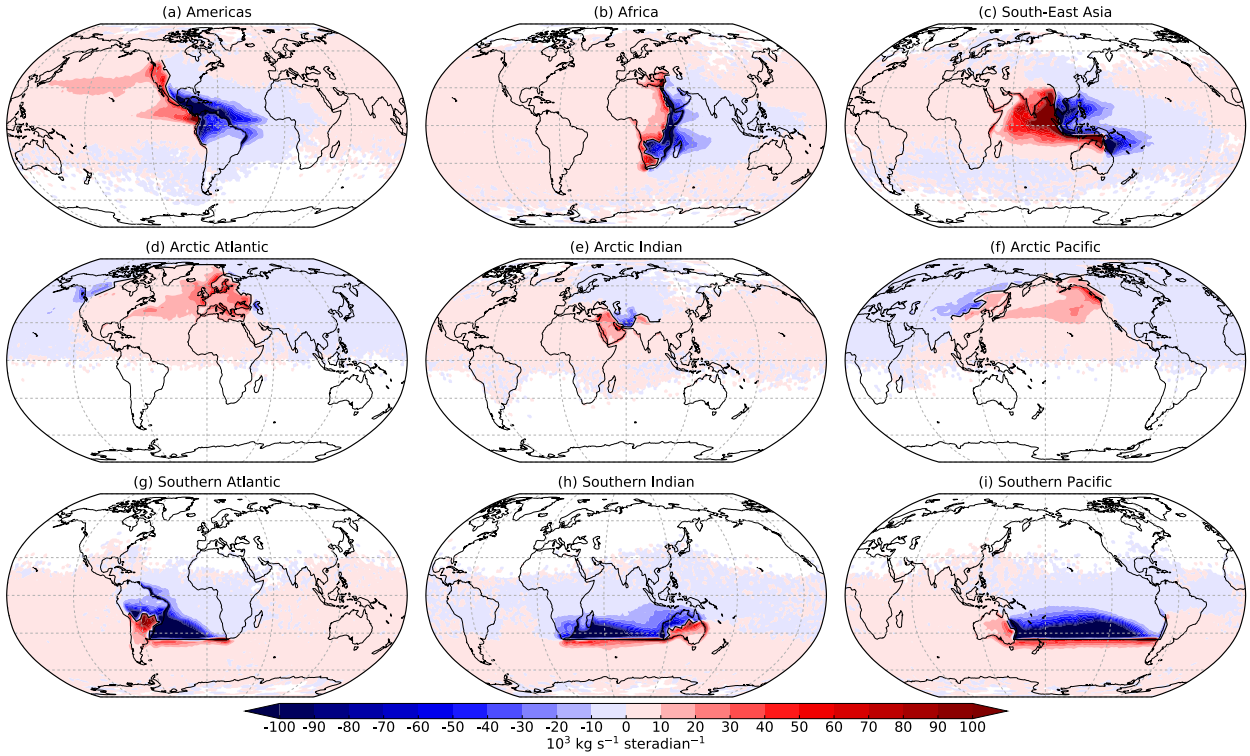


**Figure 6.** Annual mean (2010–2014) flux-weighted density maps of all origins of trajectories released from each catchment boundary (shown in black on each map). Red/positive contours indicate moisture flux in a net northward/eastward direction and blue/negative contours indicate moisture flux in a net southward/westward direction. Units are $10^3$ kg $s^{-1}$ steradian$^{-1}$.

permits air to cross into the stratosphere. In the Indian sector, the high altitude of the Himalayas also results in a higher proportion of trajectories released closer to the tropopause.

### 3.2. Flux-Weighted Density

Flux-weighted densities are generally high close to the catchment boundaries, with patterns primarily reflecting those of the origin density maps (Figure 5). However, significant differences are notable, such as the disappearance of the South Atlantic subtropical high between Figures 5h and 6h. The effect of coastal outflow can also been seen, particularly around South America (Figures 6a and 6g) where $Q_n(\mathbf{x})$ is strong along the coast. The southern hemisphere subtropical highs can be identified as approximately triangular regions with $|Q_n(\mathbf{x})| < 20 \times 10^3$ kg$^{-1}$ steradian$^{-1}$ east of regions with strong $Q_n(\mathbf{x})$ (Figures 6g–6i). The North Pacific subtropical high can be identified as the region of $Q_n(\mathbf{x}) < 20 \times 10^3$ kg$^{-1}$ steradian$^{-1}$ in Figure 6a, west of South-West North America where the annual mean moisture flux is parallel to the coast (Figure 1b).

Starting from the North, the moisture import to the Arctic is dominated by the North Atlantic and North Pacific storm tracks (wedges of high $Q_n(\mathbf{x})$ across the widths of the basins in Figures 6d and 6f), demonstrating that Arctic precipitation is mostly associated with transient moisture fluxes (Craig et al., 2020; Gimeno et al., 2019; Vazquez et al., 2016). Across the Indian sector of the Arctic catchment boundary, northward $Q_n(\mathbf{x})$ is greatest around the Arabian peninsula corresponding with regions of high $z_{\mathrm{BL}}$ and highly evaporative seas. The greatest contributions to moisture leaving the Arctic basin are found along the small section of the catchment boundaries that are north-south orientated and where westerly winds prevail.

The North Pacific storm track imports moisture into the Atlantic basin across North America and the North Atlantic storm track exports moisture across Europe (Figures 6a and 6f). High values of $Q_n(\mathbf{x})$, associated with westward $Q_n$ across Central America, are found in the Caribbean Sea and tropical North Atlantic Duran-Queseda et al. (2010) (Figure 6a). This shows that Atlantic-to-Pacific moisture transport across Central America does indeed have primary origin in this region (Broecker, 1991; Leduc et al., 2007), although this methodology cannot

directly link this flux to the location of precipitation. Note also the small import of moisture across Asia with potential origin in the North Atlantic storm track (Figure 6f). However, our analysis gives a weaker flux in the mid-latitude westerlies into the Pacific than the 0.4 Sv obtained by Dey and Döös (2020).

In the South-East Asian catchment boundary, there is a narrow band of very low $Q_n(\mathbf{x})$ off the East African coast and the Arabian peninsula highlighting the Somali Low Level Jet's (SLLJ) path (Figure 6c). The greatest $Q_n(\mathbf{x})$ for trajectories released from the South-East Asian boundary with Indian Ocean origin is found across the Bay of Bengal from trajectories released from the South-East Asian catchment boundary, and east of Madagascar from trajectories released from the Indian sector of the Southern Ocean catchment boundary.

High $Q_n(\mathbf{x})$ are found in the poleward part of the southern hemisphere subtropical highs (Figures 6g–6i). The contrasting shapes of these regions are a result of different atmospheric circulation patterns linked to the differing widths of each basin (Wills & Schneider, 2015). Moisture fluxes leaving the Southern Ocean basin have greatest $Q_n(\mathbf{x})$ close to the catchment boundary but $Q_n(\mathbf{x}) < 10$ kg s$^{-1}$ steradian$^{-1}$ are found around the Southern Ocean and much of the southern hemisphere.

## 4. Partitioning Moisture Flux Into Origin Basins

The trajectories can be used to partition $Q_{XY}$ across one catchment boundary intro contributions $\left(Q_n^i\right)$ from each drainage basin (Figure 1), from the stratosphere (*Str*) and from trajectories with no assigned origin (*none*):

$$Q_{XY} = Q_{XY}^{Atl} + Q_{XY}^{Ind} + Q_{XY}^{Pac} + Q_{XY}^{Arc} + Q_{XY}^{Sou} + Q_{XY}^{Str} + Q_{XY}^{none}. \quad (9)$$

The fluxes can be calculated either directly from trajectory model output or calculating area-integrals of each $Q_n(\mathbf{x})$ (Figure 6). The contribution from $Q_{XY}^{Str}$ (Figure 7, cyan bars) is negligible even for the Arctic which has the greatest proportion of trajectories with stratospheric origins (Table 1). The "no-origin" $Q_n^{none}$ contributions (white bars) are substantially greater than $Q_{XY}^{Str}$ but still relatively small compared to $Q_{XY}$.

$Q_{XY}$ for the American, African and South-East Asian catchment boundaries are dominated by $Q_n(\mathbf{x})$ from the two drainage basins directly adjacent to each catchment boundary. Typically, the westward contribution to the flux is larger than the eastward contribution by a factor of 2–3. The South-East Asian boundary, however, exhibits an inverse result: net $Q_{CD}$ is dominated by eastward $Q_{CD}^{Ind}$ 3–4 times stronger than the eastward fluxes across the Americas and Africa, while the westward $Q_{CD}^{Pac}$ is comparable to the westward fluxes across the Americas and Africa. These results agree with Craig et al. (2020) who showed that $Q_{CD}$ is eastward across South-East Asia, in contrast to the westward zonal moisture flux seen at other latitudes. This Lagrangian analysis shows that this contrast can be further attributed to an anomalously large eastward flux across South-East Asia.

Moisture fluxes across each sector of the Southern Ocean boundary are dominated by $Q_{XY}^{Sou}$ and $Q_{XY}^{i}$ from the ocean to the north. Contributions from other basins, albeit small, are larger than for the three meridionally orientated boundaries. The third largest contribution to $Q_{XY}$ for each sector comes from the drainage basin to the west of each sector due to the strong westerlies in the mid-latitude southern hemisphere, although the sign of this contribution is negative for the Indian sector and positive for the two other sectors. The proportions of trajectories from the tertiary source basin are not insignificantly small (Table 1) but the low $Q_{XY}^{i}$ for the tertiary sources implies these trajectories have low $q$ upon arrival at the catchment boundary.

## 5. Understanding $\overline{P-E}$ Asymmetries From Trajectory Data

The $Q_{XY}^{i}$ flux is also used to understand $\overline{P-E}$ using Equation 3 for each drainage basin (Figure 8). The estimates from trajectory model output agree reasonably well with the Eulerian estimates of $Q_{XY}$ and $\overline{P-E}$ over the same period (Figure 1). The Atlantic, Pacific and Arctic $\overline{P-E}$ from trajectory model output are very close to the values presented in Figure 1. The contrast between the Atlantic and Pacific $\overline{P-E}$ (0.44 Sv) is slightly underestimated compared to Figure 1 (0.48 Sv) but remains within error bars calculated from a range of data sources (Craig et al., 2017).

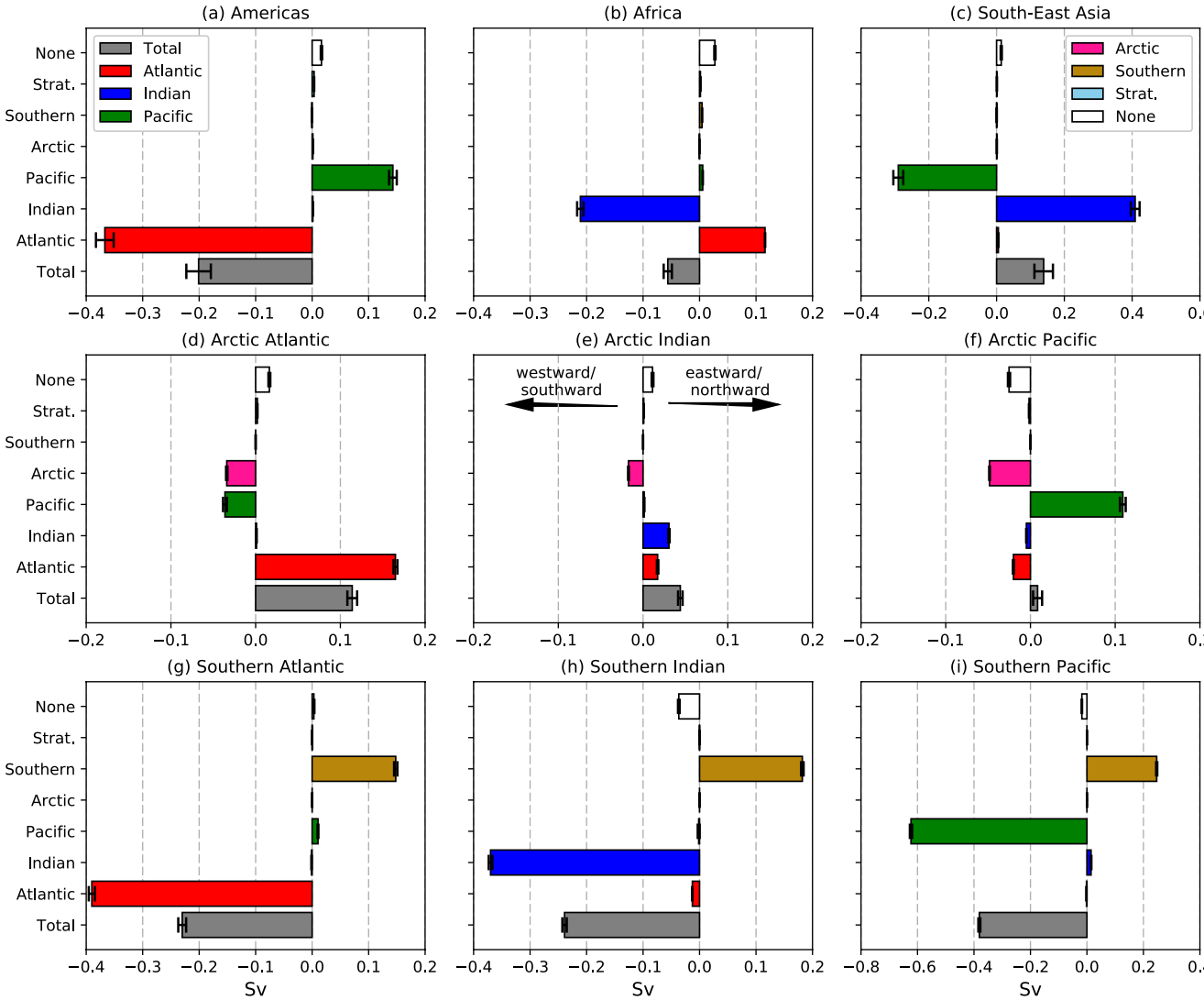


**Figure 7.** Vertically and horizontally integrated $Q_{XY}$ (2010–2014) on each catchment boundary partitioned into origin drainage basins (Atlantic, Indian, Pacific, Arctic, Southern), the stratospheric contribution and trajectories with no assigned origin. The sum of these seven $Q^{i}_{XY}$ is equal to the total $Q_{XY}$ (gray bars). All values are in Sverdrups (Sv). The error bars represent standard error of the mean. Positive fluxes represent moisture flux in a net eastward/northward direction and negative fluxes indicate moisture flux in a net westward/southward direction as labeled in panel (e).

The calculation on the trajectory arrival grid underestimates Indian Ocean $\overline{P-E}$ by 0.13 Sv. This appears to be mainly due to underestimation of $Q_{AB}$. This is likely caused by two factors:

1. Diurnal Aliasing: trajectories are only released twice daily at 00 and 12 UTC (Section 2.3) but maximum $z_{\mathrm{BL}}$ occurs between 15 and 18 UTC over Africa (Korhonen et al., 2014; Marsham et al., 2013). Therefore many trajectories were not calculated that could have been released in the BL at 18 UTC. The Turkana LLJ is also weakest at 12 UTC and strongest between 00 and 06 UTC (Nicholson, 2016), so some of the maxima in this region may not have been captured.
2. Vertical Subsampling: the vertical integrals of $qu$ and $qv$ cannot capture the near-surface and low-level flow given too large $dp$ weighting due to the relatively coarse vertical resolution of the trajectory releases (Section 2.5). This systematically occurs along all catchment boundaries where $Q_n$ peaks in low-lying regions (Figure 9b).

Southern Ocean $\overline{P-E}$ is also underestimated by the calculation on the trajectory arrival grid (Figure 8) compared to Figure 1a. This occurs all the way round the Southern Ocean catchment boundary as most of the transport is low level due to the amount of ocean directly beneath the catchment boundary. The largest discrepancy occurs

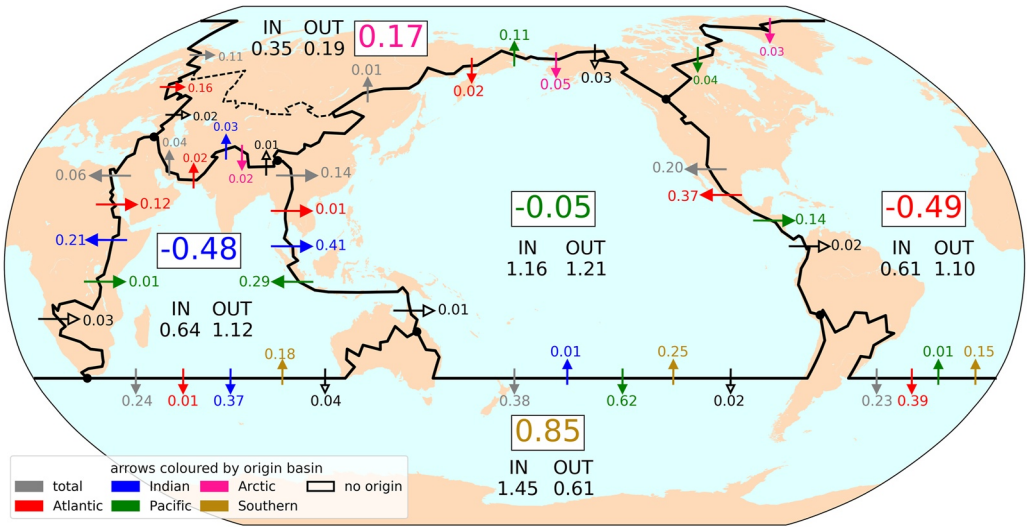


**Figure 8.** Annual mean (2010–2014) net $Q_{XY}$ (gray arrows) and contributing $Q^i_{XY}$ (other arrows) from the five drainage basins and from trajectories with no assigned moisture origin. Each arrow represents integrated values along the entire length of a catchment boundary between the two end points (dots at intersections between catchment boundaries). Also shown are the net moisture fluxes entering (IN) and leaving (OUT) each drainage basin, calculated as the sum of $Q^i_{XY}$ pointing inward and outward respectively. Note that all values are rounded two significant figures and only non-zero rounded values are displayed, so there are small discrepancies between the values of $\overline{P-E}$ (boxes) and the sum of the surrounding $Q_{XY}$ (arrows).

along the Atlantic sector (0.07 Sv) where transport into the River Plate basin is systematically underestimated (Figure 9g, gray and black lines). This may be partially due to diurnal aliasing of the South American LLJ which can peak at 06 UTC (Marengo et al., 2004).

Despite underestimating Indian Ocean $\overline{P-E}$ and African $Q_{AB}$, the calculation on the trajectory arrival grid provide an acceptable representation of the moisture budgets which can be used to understand the asymmetries between the ocean drainage basins.

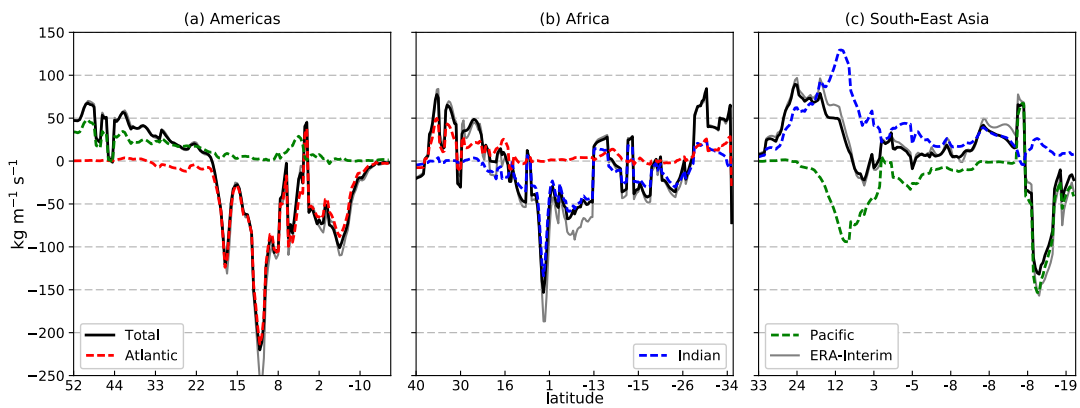


**Figure 9.** Vertically integrated $Q_n$ (2010–2014) profiles along each catchment boundary partitioned into origin drainage basins (Atlantic, Indian, Pacific, Arctic, Southern). Only the significant partitioned fluxes (Figure 7) are shown. The sum of the partitioned fluxes is approximately equal to the total moisture flux (solid black line). The thin gray line (labeled ERA-Interim) shows the annual mean $Q_n$ from the gridded monthly mean vertical integrals of $qu$ and $qv$ for the same time period to show the sensitivity of our calculations to sampling resolution. All units are kg m$^{-1}$ s$^{-1}$. Positive/negative fluxes represent flux in a eastward/northward direction and negative fluxes indicate moisture flux in a westward/southward direction.

**Table 2**
*Total Moisture Fluxes Entering (IN) and Leaving (OUT) Across the Atlantic, Indian, and Pacific Catchment Boundaries and $\overline{P-E}$ for Each Drainage Basin, All Calculated as Average Fluxes per Unit Length (Sv m$^{-1}$)*

| | Atlantic | Indian | Pacific |
|---|---|---|---|
| Area ($\times 10^{14}$ m$^2$) | 0.746 | 0.450 | 1.405 |
| Length (km) | 51,942.7 | 46,068.4 | 54,304.6 |
| IN | $1.17 \times 10^{-8}$ | $1.40 \times 10^{-8}$ | $2.13 \times 10^{-8}$ |
| OUT | $2.11 \times 10^{-8}$ | $2.44 \times 10^{-8}$ | $2.22 \times 10^{-8}$ |
| $\overline{P-E}$ | $-0.94 \times 10^{-8}$ | $-1.04 \times 10^{-8}$ | $-0.09 \times 10^{-8}$ |

*Note*. The areas of each ocean drainage basin in m$^2$ and the lengths of the catchment boundaries in km are shown in the second and third rows respectively.

### 5.1. Fluxes In/Out of Basins

The Atlantic, Pacific and Indian basins all have similar net OUT values exceeding 1 Sv (Figure 8) despite their different areas (Table 2). Pacific IN is very close to Pacific OUT, resulting in a small net $\overline{P-E}$ of 0.05 Sv. Atlantic and Indian IN fluxes are almost equal resulting in almost matching $\overline{P-E}$ values, but Indian OUT is underestimated due to underestimation of $Q_n^{Ind}$ on the African boundary. Comparing the IN and OUT fluxes as integrated values may give a biased view as the drainage basins have very different sizes. It is therefore also informative to compare the IN and OUT fluxes as length-averages around the perimeter of the drainage basins (Table 2).

The OUT fluxes per unit length have similar values (Table 2) with the Indian being slightly stronger than the other two and the Pacific the weakest. The Atlantic and Indian have similar IN fluxes per unit length but the Pacific's IN flux per unit length is about 75% and 65% stronger than the Atlantic and Indian IN fluxes respectively. Atmospheric moisture transport is therefore:

1. more efficient at importing moisture into the Pacific drainage basin than the Atlantic and Indian basins,
2. similarly efficient at exporting moisture from each of the drainage basins.

The $\overline{P-E}$ values per unit length for each basin (Table 2) therefore show that the net moisture export across the perimeter of the Pacific boundary is smaller than for the Atlantic and Indian basins by an order of magnitude.

### 5.2. Partitioned Transport Across 35°S

In Table 3, length-averaged net $Q_n$ across 2010–2014 show that moisture flux across the Atlantic sector is ~22% more efficient than moisture flux across the Pacific sector. The use of trajectories can further this analysis as each $Q_n^i$ can also be calculated as a flux per unit length (Table 3).

Partitioning $Q_n$ reveals two key parts of the contrasting length-averaged moisture fluxes. First, southward $Q_n^{Ind}$ across the Indian sector of 35°S is ~22% less efficient than $Q_n^{Atl}$ and $Q_n^{Pac}$ across their corresponding local sectors: calculated as the following ratio, for example,

$$\frac{Q_n^{Atl} - Q_n^{Ind}}{Q_n^{Atl}} \times 100, \tag{10}$$

where each $Q_n^i$ is the value from Table 3 on its corresponding local sector. This is a result of the SLLJ in JJA which causes anomalous cross-equatorial moisture transport from the southern hemisphere subtropical high, thus diverting moisture transport equatorwards rather than polewards in the southern hemisphere Indian sector.

The second part of the contrast in net length-averaged $Q_n$ comes from the northward $Q_n^{Sou}$ across 35°S which is least efficient across the Atlantic sector. Along 35°S much of the Atlantic basin is occupied by the poleward part of the subtropical high with a much smaller fraction of the basin covered by the equatorward part of the subtropical high compared to the Pacific and Indian sectors (Figure 1b). Northward $Q_n^{Atl}$ across 35°S is therefore severely restricted.

**Table 3**
*Total $Q_n$ and Moisture Fluxes per Unit Length Partitioned by the Basin of Origin Denoted by Index i per Unit Length (in $10^{-8}$ Sv m$^{-1}$, Rounded to 2 Significant Figures) Across 35°S for Each Sector of the Southern Ocean Catchment Boundary*

| | $Q_n$ | $Q_n^{Atl}$ | $Q_n^{Ind}$ | $Q_n^{Pac}$ | $Q_n^{Sou}$ |
|---|---|---|---|---|---|
| Atlantic sector | −3.51 | −4.42 | −0.02 | −0.07 | 1.37 |
| Indian sector | −2.03 | −0.13 | −3.46 | 0.00 | 1.74 |
| Pacific sector | −2.88 | 0.00 | −0.03 | −4.48 | 1.78 |

### 5.3. Partitioning $P-E$

Similarly to $Q_n$, $P-E$ can also be partitioned into contributions from origin drainage basins through an equation analogous to Equation 9:

$$P-E = (P-E)^{Atl} + (P-E)^{Ind} + (P-E)^{Pac} + (P-E)^{Arc} + (P-E)^{Sou} + (P-E)^{Str} + (P-E)^{none}, \tag{11}$$

where each $(P-E)^i$ is calculated from Equation 3 using the associated $Q_{XY}^i$ from Figure 7. Each basin's contribution to its own $P-E$ is approximately

**Table 4**
*Contributions to Total $\overline{P-E}$ for Each Drainage Basin From Moisture Fluxes From Trajectories With Origin in Each Drainage Basin and Trajectories With No Origin in 14 Days*

| | | Drainage basins | | | | |
|---|---|---|---|---|---|---|
| | | Atlantic | Indian | Pacific | Arctic | Southern |
| $\left(\overline{P-E}\right)^i$ | Atlantic | −1.04 | 0.08 | 0.39 | 0.16 | 0.4 |
| | Indian | 0.21 | −1.02 | 0.43 | 0.03 | 0.36 |
| | Pacific | 0.18 | 0.29 | −1.16 | 0.07 | 0.61 |
| | Arctic | 0.03 | 0.02 | 0.05 | −0.10 | 0.00 |
| | Southern | 0.15 | 0.19 | 0.25 | 0.00 | −0.58 |
| | None | −0.03 | −0.03 | 0.00 | 0.00 | 0.05 |

*Note*. Contributing $\overline{P-E}$ are denoted $\left(\overline{P-E}\right)^i$ (rows, $i$ represents origin basins) and shown to 2 significant figures in Sv. The $\left(\overline{P-E}\right)^i$ from trajectories with stratospheric origin are too small to be included. Each $\left(\overline{P-E}\right)^i$ is calculated from the corresponding $Q^i_{XY}$ on all catchment boundaries surrounding the drainage basin from Figure 7. The columns indicate the drainage basins for which each $\overline{P-E}$ is calculated.

equal to its OUT flux (Figure 8) but there can be a small contribution from $(P-E)^{none}$ (Table 4).

The key result from partitioning $\overline{P-E}$ is that Pacific $\overline{P-E}$ is dominated by $(P-E)^{Ind}$ which accounts for approximately 35% of Pacific IN (Figure 8). Contributions from $(P-E)^{Atl}$ and $(P-E)^{Sou}$ are significant but secondary to $(P-E)^{Ind}$. Therefore trajectories with Indian basin origin induce a net precipitation of 0.43 Sv across the Pacific Ocean, similar to Stohl and James (2005). The $Q_n^{Ind}$ crossing South-East Asia (0.41 Sv, Figure 8) also accounts for 37% of the Indian basin OUT flux, whereas eastward $Q_{AB}^{Atl}$ and $Q_{EF}^{Pac}$ only account for ∼11% of their associated OUT fluxes. This highlights how anomalous eastward moisture fluxes across South-East Asia (Ferreira et al., 2018) affect Pacific and Indian $\overline{P-E}$, and is also the leading cause of the Pacific/Atlantic and Pacific/Indian $\overline{P-E}$ asymmetries.

## 6. Key Dynamical Processes Influencing $\overline{P-E}$ Asymmetries

In this section the trajectories will be used to highlight the dominant dynamical processes affecting $Q_n$ and the locations where the strongest $Q_n$ are found with respect to the $\overline{P-E}$ asymmetry. This section focuses on $Q_n$ along the three meridional catchment boundaries since deviations from zonal-mean zonal moisture flux along these boundaries are the most important for the existence of the $\overline{P-E}$ asymmetries (Craig et al., 2020).

### 6.1. Peaks in $Q_n$

Since trajectories were released on 17 vertical levels, we can calculate profiles of vertically-integrated $Q_n$ (Figure 9) and cross-sections (Figure 10) along the catchment boundaries. This makes it possible to identify the horizontal and vertical locations of the $Q_n$ peaks and then to link them to dynamical features.

Atlantic-to-Pacific transport across the Americas is dominated by westward $Q_n^{Atl}$ south of 20°N (Figures 9a and 10a). The $Q_n^{Atl}$ profile is characterized by three distinct maxima in Central America associated with gap winds through the orography with the peak at 11°N above Lake Nicaragua in the Papagayo jet (Clarke, 1988). The maxima occur between 850 and 900 hPa, the approximate pressure levels of these gap winds, similar to cross-sections of velocity, water vapor mixing ratio and moisture transport anomalies (Xu et al., 2005; Yang et al., 2021). This demonstrates the smaller role of moisture transport above Panama compared to its neighbors

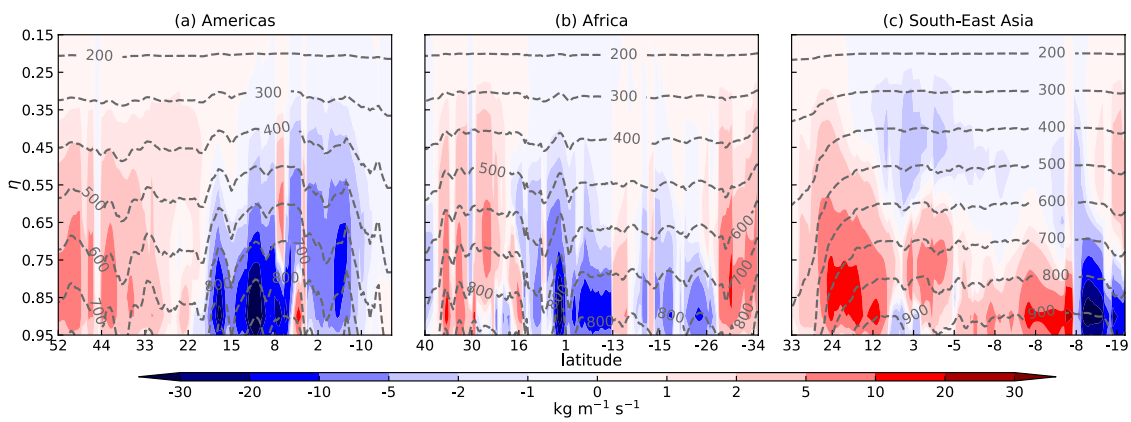


**Figure 10.** Cross-sections of $Q_n$ (in kg m$^{-1}$ s$^{-1}$, not weighted by d$l$) for each catchment boundary (2010–2014) from trajectory output on model $\eta$ levels. Positive contours indicate moisture flux in a northward/eastward direction and negative contours indicate moisture flux in a southward/westward direction. The cross-sections in panels (a)–(c) are plotted as a function of latitude along the catchment boundaries and the cross-sections in panels (d)–(i) are plotted as a function of longitude along the catchment boundaries. The dashed gray lines show the pressure levels in hPa.

further north in this region despite some studies (Leduc et al., 2007; Lohmann, 2003; Sinha et al., 2012; Zaucker & Broecker, 1992) previously assuming that this moisture flux was the key reason for the contrasting Pacific and Atlantic $\overline{P-E}$ values.

Across Africa, Indian-to-Atlantic $Q_n$ is dominated by westward $Q_n^{Ind}$ between 20°N and 26°S (Figures 9b and 10b). The $Q_n^{Ind}$ peak occurs at 3°N in the Turkana Channel and at 850–875 hPa which is the same level as the Turkana LLJ (Nicholson, 2016). South of the Turkana Channel, $Q_n^{Ind}$ is approximately $-50$ kg m$^{-1}$ s$^{-1}$ at 750 hPa until 13°S (above the African Great Lakes). This is linked to moisture transport from the Indian Ocean to the Ethiopian Highlands (Viste & Sorteberg, 2011). The eastward $Q_n^{Atl}$ is much weaker than $Q_n^{Ind}$ with a peak near 35°N above the Middle East and extends higher in altitude up to 300 hPa.

The profile of Pacific-to-Indian $Q_n$ across South-East Asia is dominated by eastward $Q_n^{Ind}$ that causes deviations from $\left[\overline{qu}\right]$ (Craig et al., 2020) while westward $Q_n^{Pac}$ only dominates above the Torres Strait (Figures 9c and 10c). The westward moisture flux in the $Q_n$ cross-section at 600–300 hPa between 3°N and 5°S is caused by the upper branch of the Walker Circulation (Figure 10c) over the Indian Ocean. The core of the eastward transport into the Pacific occurs between 12°N and 24°N below 600 hPa across Thailand and Burma.

### 6.2. Seasonal Cycles of $Q^i_{XY}$

Some of the processes discussed in Section 6.1 are strongly seasonal. Figure 11 shows the seasonal cycles of $Q_{XY}$ and the $Q^i_{XY}$ contributions from the two adjacent drainage basins. The key result is that the seasonal cycles of $Q_{XY}^{Ind}$ dominates the seasonal cycle of $Q_{AB}$ and $Q_{CD}$.

The seasonal cycles of moisture origins for the African and South-East Asian boundaries (Figure 12) show that the seasonal cycles of each season's $Q_{CD}^{Ind}$ are closely linked to the SLLJ dynamics and the Asian Monsoon. The meridional (cross-equatorial) SLLJ branch forms in April/May (Riddle & Cook, 2008) and transports moisture from the Indian Ocean near Madagascar toward East Africa (Figure 12). In June, the zonal SLLJ branch forms and diverts moisture eastwards away from the Horn of Africa toward the monsoon rains over India causing a reduction in $Q_{AB}^{Ind}$ of ~0.1 Sv from MAM to JJA (Figure 11b) with $Q_n(\mathbf{x})$ retreating across the Horn of Africa and adjacent ocean (Figure 12) linked to the seasonal cycle of East African rainfall (Liebmann et al., 2012; Wainwright et al., 2019). The seasonal reversal of winds and vertically-integrated moisture fluxes result in the South-East Asian $Q_n^{Ind}$ origin region expanding across the Indian Ocean from DJF to JJA (Figure 12) and therefore the change in sign of $Q_{CD}$.

The seasonal cycle of moisture fluxes leaving the Indian Ocean drainage basin across Africa and South-East Asia is therefore strongly affected by the continental geometry and topographic features of the basin. Land-sea temperature contrasts are considered to play a role in the seasonal reversal of surface winds, as is the Intertropical Convergence Zone (ITCZ's) seasonal migration (Bordoni & Schneider, 2008; Gadgil, 2003). As the ITCZ moves northward the East African Highlands and land-sea friction contrasts concentrate the SLLJ into a narrow longitudinal band (Rodwell & Hoskins, 1995). The difference between the atmospheric dynamics in January and June can be seen from the trajectories in Figure 4b with a fully formed SLLJ dominating the lower troposphere in June and nonexistent in January (Dey & Döös, 2021; Volonté et al., 2019). Most origins for South-East Asian $Q_n^{Ind}$ are not located directly below the SLLJ but instead along the coast, or to the south, of India (Figure 4b) where the trajectories exit the BL or experience mixing. However, Rodwell and Hoskins (1995) estimated that 60%–80% of moisture transported by the SLLJ is from the southern hemisphere subtropical high. Stojanovic et al. (2021) showed that the Bay of Bengal is the most important moisture source for part of South-East Asia during the dry season (May–October) and the South China Sea is the most important moisture source during the dry season (November–April), consistent with the flux-weighted density maps in Figure 12.

The seasonal cycle of Americas $Q_{AB}$ is dominated by westward $Q_{AB}^{Atl}$ which peaks in JJA (Figure 11a). The $Q_{AB}^{Atl}$ origin region extends across the tropical Atlantic onto North Africa with $Q_n(\mathbf{x}) > 10^5$ kg s$^{-1}$ steradian$^{-1}$ over the Caribbean Sea (Figure 12). The dominant dynamical feature affecting the seasonal cycle of $Q_{AB}^{Atl}$ is the Caribbean LLJ (CLLJ) which is strongest in JJA due to the meridional sea level pressure gradient with the North Atlantic subtropical high (Wang et al., 2007). The Atlantic Warm Pool does not appear to influence the seasonal cycle of $Q_{AB}^{Atl}$ quite as strongly since it peaks in September (Wang & Enfield, 2001) and is likely to inhibit moisture transport from the Atlantic across Central America due to anomalous low-level convergence associated with sea surface temperature anomalies (Wang et al., 2013).

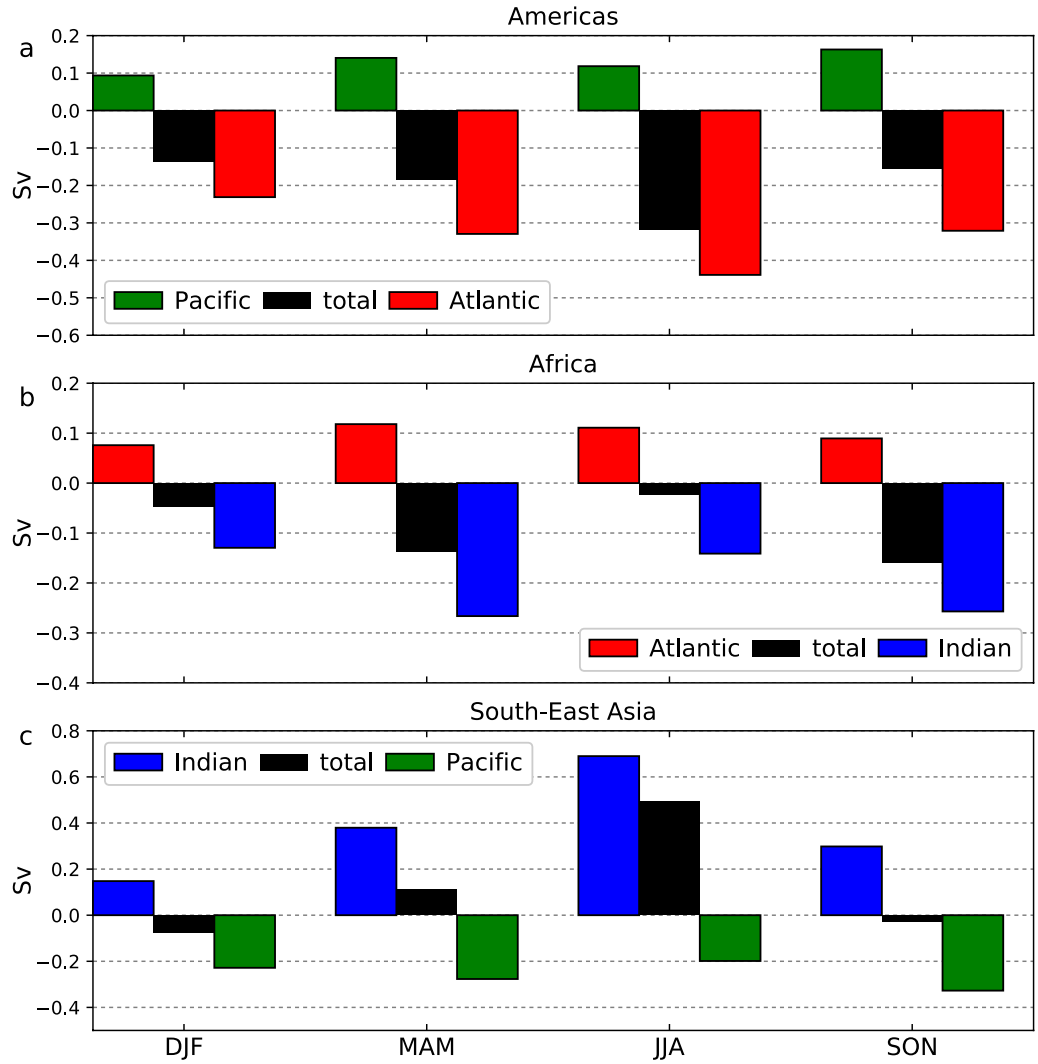


**Figure 11.** Vertically and horizontally integrated 2010–2014 climatological seasonal mean $Q_{XY}$ for the (a) American, (b) African, and (c) South-East Asian catchment boundaries. The $Q_{XY}$ (black) and $Q^{i}_{XY}$ from trajectories with origin in the two adjacent basins to each catchment boundary are shown (Atlantic: red, Pacific: green, Indian: blue). Positive $Q_{XY}$ indicates moisture flux in a net eastward direction and negative $Q_{XY}$ indicates moisture flux in a net westward direction. These values (in Sv) are calculated from $Q_n(\mathbf{x})$ in Figure 12.

The effect of the CLLJ is shown by the densely packed origins across the Caribbean Sea associated with the low-level trajectories from the North Atlantic subtropical high or zonal mid-tropospheric flow across the tropical North Atlantic. Most of the trajectories associated with the CLLJ have Atlantic origin (Figure 4c), but some cross Central America without making contact with the BL or experiencing sufficient mixing until they are above the Pacific basin. Such trajectories undergo cyclonic curvature caused by interaction with the Panama Low (Mesa-Sánchez & Rojo-Hernández, 2020), therefore contributing toward westward $Q^{Pac}_{AB}$ across the Andes and reducing Atlantic net evaporation. This extension of the CLLJ combines with the Choco LLJ at 5°N (Figure 4d) which, after crossing the equator, undergoes cyclonic curvature, resulting in heavy precipitation in the Colombian Andes (Mejía et al., 2021; Poveda et al., 2014).

The dominant dynamical features influencing moisture fluxes associated with the $\overline{P-E}$ asymmetries are therefore the SLLJ and subsequent eastward flow toward South-East Asia—both of which are associated with the continental geometry and topographic features of the Indian Ocean basin. In JJA eastward moisture fluxes across India and the Bay of Bengal toward the South-East Asian catchment boundary dominate annual mean $Q_{CD}$ and therefore Indian and Pacific $\overline{P-E}$. This results in the anomalies from $\left[\overline{qu}\right]$ that dominate the annual mean

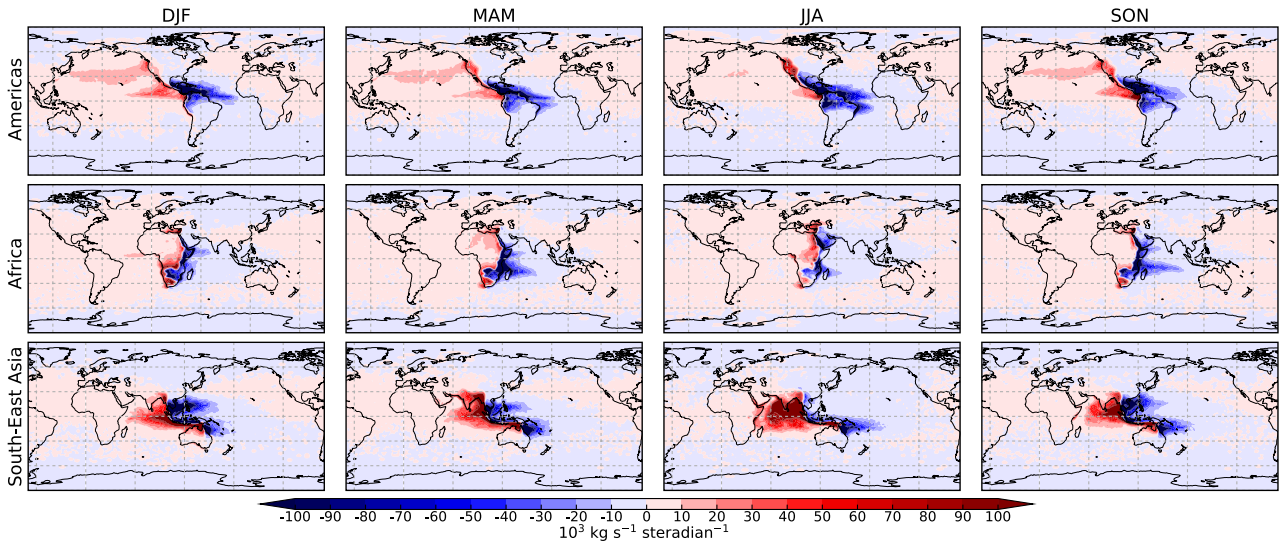


**Figure 12.** Flux-weighted density maps for the 2010–2014 climatological seasonal means of all trajectories with CAT I and CAT II origins released from the American (top row), African (middle row) and South-East Asian (bottom row) catchment boundaries. Red/positive contours indicate moisture fluxes crossing the catchment boundaries in an eastward direction and blue/negative contours indicate moisture fluxes crossing the catchment boundaries in a westward direction. Units are $10^3$ kg $s^{-1}$ steradian$^{-1}$.

Pacific/Atlantic and Pacific/Indian $\overline{P-E}$ asymmetries. The CLLJ dominates the seasonal cycle of American $Q_{AB}^{Atl}$ and therefore plays an important role in the seasonal cycle of Atlantic $\overline{P-E}$, but it makes a far less significant contribution to Pacific net precipitation.

## 7. Conclusions

Previous work has shown how seasonal and interannual variability in the atmospheric water budget over an ocean basin, summarized by precipitation minus evaporation ($P-E$) on averaging over a season, can be related to the variability in the moisture fluxes normal to the boundaries defining each region (Craig et al., 2020). Furthermore, the differences in net $P-E$ over the Pacific, Atlantic and Indian Ocean basins can be explained in terms of the seasonal moisture fluxes and relation to flow features. In particular, the Atlantic and Indian Ocean have net negative $P-E$, while the Pacific Ocean has near neutral $P-E$, and this can be attributed in part to the anomalous moisture flux in the Asian Summer Monsoon between the Indian and Pacific Ocean basins. However, calculation of the moisture flux alone is not sufficient to determine where the water has come from and how evaporation from one ocean contributes to precipitation over another. In this paper, we take the approach further by partitioning the moisture flux across each catchment boundary in terms of the origins of the water that contributes to the flux. In this way water can be traced from one basin to another and the results used to determine how important each basin is to the variability in $P-E$ integrated over another ocean.

The ocean basin catchment boundaries are defined using the watersheds along the continents between the ocean basins as well as some lines across ocean sections that complete the partitions between the ocean basins where necessary (see Figure 1a). Moisture fluxes normal to the boundaries were calculated using ERA-Interim data on a 12-hourly basis. An airmass trajectory model (Methven, 1997) was used to release 14-day back trajectories from the catchment boundaries surrounding each ocean drainage basin and the "moisture origin" of each trajectory was determined using the method of de Leeuw et al. (2017). In this way, the moisture fluxes across each boundary between catchments can be partitioned, attributing the flux contributions to the basins of origin. This provides a complete network of transports between the five ocean basins (Pacific, Atlantic, Indian, Arctic, and Southern Oceans—Figure 8) plus the stratosphere and moisture fluxes associated with origins that could not be determined with 14-day back trajectories (a contribution to the moisture fluxes of <15%). Summarizing the main results:

1. The majority of moisture contributing to fluxes across a boundary originates near the boundary. Previous studies (Broecker, 1991; Leduc et al., 2007; Zaucker & Broecker, 1992) have implicitly or explicitly assumed that Atlantic-to-Pacific moisture crossing Central America in the easterly trade winds has Atlantic origin

without considering remote sources. Our results show that this assumption is broadly correct because $q$ is highest in the BL where lower tropospheric transport is slow and the greatest $Q_n(\mathbf{x})$ are found along or close to the catchment boundaries from which trajectories are released (Figure 6).

Partitioning $Q_n$ into contributions from origin drainage basins therefore shows that the $Q^i_{XY}$ from the basins directly adjacent to the three meridional catchment boundaries and each sector of the Southern Ocean catchment boundary dominates $Q_{XY}$ (Figure 7). Trajectories with remote or stratospheric origin (that are generally released at higher altitudes) have very low moisture content upon arrival at the catchment boundary so make negligible contributions to $Q_{XY}$. Tertiary sources are more important for the three sectors of the Arctic catchment boundary with $Q^i_{XY}$ values comparable to the primary northward $Q^i_{XY}$ from the basin directly south of the catchment boundary and southward $Q^{Arc}_{XY}$.

2. The Pacific imports moisture with greater efficiency. The Lagrangian approach allows the net fluxes across the catchment boundaries, $Q_n$, to be partitioned into leaving and entering contributions (Figure 8). The atmosphere exports similar quantities of moisture (slightly greater than 1 Sv) from the Atlantic, Indian and Pacific basins. Approximately the same quantity is imported to the Pacific basin, giving it a near-neutral $\overline{P-E}$. However, the moisture imports are only slightly over half of the exports in the Atlantic and Indian basins resulting in strong negative $\overline{P-E}$ in these two basins. The imported and exported moisture fluxes per unit length around the perimeters of their catchment boundaries (Table 2) show that atmospheric moisture import around the Pacific basin is almost double the values of the flux per unit length across the perimeters of the Atlantic and Indian basins while all three basins have approximately equal export efficiency. This is consistent with the similar values of area-averaged evaporation for each basin but stronger area-averaged precipitation for the Pacific than for the Atlantic and Indian Oceans (Craig et al., 2017).

3. Each basin's $\overline{P-E}$ can be partitioned into contributions associated with the fluxes around the basin perimeter. Pacific $\overline{P-E}$ is dominated by trajectories with Indian Ocean origin, which accounts for 38% of the Pacific import flux and therefore associated with 0.43 Sv net precipitation over the Pacific (similar to Stohl and James (2005)). The $Q^{Ind}_n$ across South-East Asia is approximately 38% of the Indian OUT value compared to ∼11% of the Atlantic and Pacific OUT fluxes from their respective eastward exports across their eastern boundaries.

   Craig et al. (2020) suggested that the shapes of the southern hemisphere subtropical highs and the fractions of the ocean basins they occupy influences atmospheric moisture transport to and from the Southern Ocean basin. Partitioning $Q_n$ shows that northward $Q^{Sou}_n$ along 35°S is weakest on the Atlantic sector by about 22% compared to the Indian and Pacific sectors resulting in a strong net southward $Q_n$. This contributes to the strong $\overline{P-E} < 0$ of the Atlantic basin and is a consequence of Atlantic Ocean's narrowness at 35°S since a greater fraction of the basin is occupied by the poleward part of the subtropical high compared to the other two basins. Partitioning $Q_n$ also shows that southward export across 35°S is weaker (by ∼22%) in the Indian sector than in the Atlantic and Pacific sectors. This is caused by the SLLJ presence in JJA which diverts moisture from the southern hemisphere subtropical high and causes anomalous cross-equatorial moisture transport from the southern hemisphere (Rodwell & Hoskins, 1995).

4. The SLLJ and monsoon explain the larger Pacific area-averaged precipitation. Our results confirm Craig et al. (2020)'s finding that Panama is not the prime location for Atlantic-to-Pacific moisture transport. The pressure levels associated with cross-boundary fluxes are linked to the LLJs identified by Craig et al. (2020) as well as to the Walker Circulation.

   Maps of $Q_n(\mathbf{x})$ (Figure 6) support Craig et al. (2020)'s hypothesis that the SLLJ diverts the moisture flux away from Africa toward India in JJA (Figure 4b). Westerly winds carry moisture across the Bay of Bengal where trajectories undergo substantial moistening (Figure 12) toward South-East Asia resulting in large eastward $Q^{Ind}_n$ to the Pacific basin. The Indian-to-Pacific moisture transport accounts for approximately 38% of atmospheric moisture entering the Pacific and dominates Pacific $\overline{P-E}$ (Table 4). Trajectories with Indian Ocean origin are therefore the leading cause of the greater precipitation per unit area across the Pacific Ocean compared to the Atlantic and Indian Oceans (Craig et al., 2017; Stohl & James, 2005) and this atmospheric moisture transport dominates the $\overline{P-E}$ asymmetries.

   These results support the interpretation from Stohl and James (2005)'s forward trajectory study for understanding precipitation origins and from Emile-Geay et al. (2003) that the Asian Monsoon causes the contrasting levels of Pacific and Atlantic subpolar precipitation. Czaja (2009) also linked monsoonal moisture transport to contrasting Pacific and Atlantic salinity and $\overline{P-E}$ patterns. However, our findings contrast Dey and

Döös (2020) who attributed the $\overline{P-E}$ asymmetries to Atlantic-to-Pacific moisture transport in the midlatitude westerlies. By considering each of the five ocean drainage basins individually and using the de Leeuw et al. (2017) method for attributing moisture origins in airmass trajectories, we have provided detailed quantitative evidence for the role of the SLLJ and South Asian Monsoon in anomalous eastward Indian-to-Pacific atmospheric moisture transport in agreement with previous Eulerian analysis (Craig et al., 2017, 2020) and verified the hypotheses of Craig et al. (2020).

Topographic features and continental geometry are therefore a key part of the $\overline{P-E}$ asymmetries. African topography has been shown to play a key role in the strength of the SLLJ (Rodwell & Hoskins, 1995; Wei & Bordoni, 2016). The widths of the ocean basins (Ferreira et al., 2010; Schmitt et al., 1989) also affect the $\overline{q}\,\overline{v}$ patterns since the subtropical highs occupy different fractions of the basin widths, thus affecting both poleward and equatorward moisture fluxes.

## Data Availability Statement

The ERA-Interim data set is available from the Copernicus Climate Change Service (C3S) Climate Data Store (https://cds.climate.copernicus.eu/cdsapp#!/dataset/reanalysis-era-interim?tab=overview; ECMWF, 2011). The ROTRAJ model code is available at https://www.met.reading.ac.uk/~swrmethn/ROTRAJ/ (Methven, 1997). An example of the trajectory output data is available from the University of Reading Research Data Repository at https://doi.org/10.17864/1947.000461 (Craig, 2023).

**Acknowledgments**
The lead author received PhD studentship funding from the Natural Environment Research Council as part of the SCENARIO Doctoral Training Partnership (NE/L002566/1).

## References

Baker, A., Sodemann, H., Baldini, J., Breitenbach, S., Johnson, K., van Hunen, J., & Pingzhong, Z. (2015). Seasonality of westerly moisture transport in the East Asian Summer Monsoon and its implications for interpreting precipitation $\delta^{18}$O. *Journal of Geophysical Research: Atmospheres*, *120*(12), 5850–5862. https://doi.org/10.1002/2014jd022919

Berrisford, P., Kållberg, P., Kobayashi, S., Dee, D., Uppala, S., Simmons, A., et al. (2011). Atmospheric conservation properties in ERA-Interim. *Quarterly Journal of the Royal Meteorological Society*, *137*(659), 1381–1399. https://doi.org/10.1002/qj.864

Bolton, D. (1980). The computation of equivalent potential temperature. *Monthly Weather Review*, *108*(7), 1046–1053. https://doi.org/10.1175/1520-0493(1980)108<1046:tcoept>2.0.co;2

Bordoni, S., & Schneider, T. (2008). Monsoons as eddy-mediated regime transitions of the tropical overturning circulation. *Nature Geoscience*, *1*(8), 515–519. https://doi.org/10.1038/ngeo248

Broecker, W. (1991). The Great Ocean conveyor. *Oceanography*, *4*(2), 79–89. https://doi.org/10.5670/oceanog.1991.07

Clarke, A. (1988). Inertial wind path and sea surface temperature patterns near the Gulf of Tehuantepec and the Gulf of Papagayo. *Journal of Geophysical Research*, *93*(C12), 15491–15501. https://doi.org/10.1029/jc093ic12p15491

Craig, P. (2019). Catchment boundaries of ocean drainage basins [Dataset]. University of Reading. https://doi.org/10.17864/1947.195

Craig, P. (2023). Back trajectories released from ocean catchment boundaries [Dataset]. University of Reading. https://doi.org/10.17864/1947.000461

Craig, P., Ferreira, D., & Methven, J. (2017). The contrast between Atlantic and Pacific surface water fluxes. *Tellus A*, *69*(1), 1330454. https://doi.org/10.1080/16000870.2017.1330454

Craig, P., Ferreira, D., & Methven, J. (2020). Monsoon-induced zonal asymmetries in moisture transport cause anomalous Pacific precipitation minus evaporation. *Geophysical Research Letters*, *47*, e2020GL088659. https://doi.org/10.1029/2020gl088659

Czaja, A. (2009). Atmospheric control on the thermohaline circulation. *Journal of Climate*, *39*(1), 234–247. https://doi.org/10.1175/2008jpo3897.1

Dacre, H., Gray, S., & Belcher, S. (2007). A case study of boundary layer ventilation by convection and coastal processes. *Journal of Geophysical Research*, *112*(D17), D17106. https://doi.org/10.1029/2006jd007984

Dee, D., Uppala, S., Simmons, A., Berrisford, P., Poli, P., Kobayashi, S., et al. (2011). The ERA-interim reanalysis: Configuration and performance of the data assimilation system. *Quarterly Journal of the Royal Meteorological Society*, *137*(656), 553–597. https://doi.org/10.1002/qj.828

de Leeuw, J., Methven, J., & Blackburn, M. (2017). Physical factors influencing regional precipitation variability attributed using an airmass trajectory method. *Journal of Climate*, *30*(18), 7359–7378. https://doi.org/10.1175/jcli-d-16-0547.1

Dey, D., Campino, A., & Döös, K. (2023). Atmospheric water transport connectivity within and between ocean basins and land. *Hydrology and Earth System Sciences*, *27*(2), 481–493. https://doi.org/10.5194/hess-27-481-2023

Dey, D., & Döös, K. (2020). Atmospheric freshwater transport from the Atlantic to the Pacific Ocean: A Lagrangian analysis. *Geophysical Research Letters*, *47*(6), e2019GL086176. https://doi.org/10.1029/2019gl086176

Dey, D., & Döös, K. (2021). Tracing the origin of the South Asian Summer Monsoon precipitation and its variability using a novel Lagrangian framework. *Journal of Climate*, *34*(21), 8655–8668. https://doi.org/10.1175/jcli-d-20-0967.1

Duran-Queseda, A., Gimeno, L., Amador, J., & Nieto, R. (2010). Moisture sources for Central America: Identification of moisture sources using a Lagrangian analysis technique. *Journal of Geophysical Research*, *115*, D05103. https://doi.org/10.1029/2009jd012455

ECMWF. (2011). ERA-interim global atmospheric reanalysis [Dataset]. Copernicus Climate Change Service (C3S) Climate Data Store (CDS). https://doi.org/10.24381/cds.f2f5241d

ECMWF. (2015). IFS documentation Cy41r1, Part IV: Physical processes. Online. Retrieved from https://www.ecmwf.int/en/elibrary/9211-part-iv-physical-processes

Emile-Geay, J., Cane, M., Naik, N., Seager, R., Clement, A., & van Geen, A. (2003). Warren revisited: Atmospheric freshwater fluxes and "Why is no deep water formed in the North Pacific". *Journal of Geophysical Research*, *108*(C6), 3178. https://doi.org/10.1029/2001jc001058

Emmanuel, K. (1994). *Atmospheric convection*. Oxford University Press.

Ferreira, D., Cessi, P., Coxall, H., de Boer, A., Dijkstra, H., Drijfhout, S., et al. (2018). Atlantic-Pacific asymmetry in deep water formation. *Annual Review of Earth and Planetary Sciences*, *46*(1), 327–352. https://doi.org/10.1146/annurev-earth-082517-010045

Ferreira, D., Marshall, J., & Campin, J.-M. (2010). Localization of deep water formation: Role of atmospheric moisture transport and geometrical constraints on ocean circulation. *Journal of Climate*, *23*(6), 1456–1476. https://doi.org/10.1175/2009jcli3197.1

Gadgil, S. (2003). The Indian Monsoon and its variability. *Annual Review of Earth and Planetary Sciences*, *31*(1), 429–467. https://doi.org/10.1146/annurev.earth.31.100901.141251

Gimeno, L., Drumond, A., Nieto, R., Trigo, R., & Stohl, A. (2010). On the origin of continental precipitation. *Geophysical Research Letters*, *37*, L13804. https://doi.org/10.1029/2010gl043712

Gimeno, L., Vázquez, M., Eiras-Barca, J., Sorí, R., Algarra, I., & Nieto, R. (2019). Atmospheric moisture transport and the decline in Arctic sea ice. *WIRES Climate Change*, *10*, e588. https://doi.org/10.1002/wcc.588

Hodges, K. (1996). Spherical nonparametric estimators applied to the UGAMP model integration for AMIP. *Monthly Weather Review*, *124*(12), 2914–2932. https://doi.org/10.1175/1520-0493(1996)124<2914:sneatt>2.0.co;2

Korhonen, K., Giannakaki, E., Mielonen, T., Pfüller, A., Laakso, L., Vakkari, V., et al. (2014). Atmospheric boundary layer top height in South Africa: Measurements with lidar and radiosonde compared to three atmospheric models. *Atmospheric Chemistry and Physics*, *14*(8), 4263–4278. https://doi.org/10.5194/acp-14-4263-2014

Läderach, A., & Sodemann, H. (2016). A revised picture of the atmospheric moisture residence time. *Geophysical Research Letters*, *43*(2), 924–933. https://doi.org/10.1002/2015gl067449

Leduc, G., Vidal, L., Tachikawa, K., Rostek, F., Sonzogni, C., Beaufort, L., & Bard, E. (2007). Moisture transport across Central America as a positive feedback on abrupt climatic changes. *Nature*, *445*(7130), 908–911. https://doi.org/10.1038/nature05578

Liebmann, B., Bladé, I., Kiladis, G., Carvalho, L., Senay, G., Allured, D., et al. (2012). Seasonality of African precipitation from 1996 to 2009. *Journal of Climate*, *25*(12), 4304–4322. https://doi.org/10.1175/jcli-d-11-00157.1

Lohmann, G. (2003). Atmospheric and oceanic freshwater transport during weak Atlantic overturning circulation. *Tellus A*, *55*(5), 438–449. https://doi.org/10.1034/j.1600-0870.2003.00028.x

Marengo, J., Soares, W., Saulo, C., & Nicolini, M. (2004). Climatology of the low-level jet east of the Andes as derived from the NCEP–NCAR reanalyses: Characteristics and temporal variability. *Journal of Climate*, *17*(12), 2261–2280. https://doi.org/10.1175/1520-0442(2004)017<2261:cotlje>2.0.co;2

Marsham, J., Hobby, M., Allen, C., Banks, J., Bart, M., Brooks, B., et al. (2013). Meteorology and dust in the central Sahara: Observations from Fennec supersite-1 during the June 2011 intensive observation period. *Journal of Geophysical Research: Atmospheres*, *118*(10), 4069–4089. https://doi.org/10.1002/jgrd.50211

Mejía, J., Yepes, J., Henao, J., Poveda, G., Zuluaga, M., Raymond, D., & Fuchs-Stone, Z. (2021). Towards a mechanistic understanding of precipitation over the far eastern Tropical Pacific and Western Colombia, One of the rainiest spots on earth. *Journal of Geophysical Research: Atmospheres*, *126*, e2020JD033415. https://doi.org/10.1029/2020jd033415

Mesa-Sánchez, O., & Rojo-Hernández, J. (2020). On the general circulation of the atmosphere around Colombia. *Revista de la Academia Colombiana de Ciencias Exactas, Físicas y Naturales*, *44*(172), 857–875. https://doi.org/10.18257/raccefyn.899

Methven, J. (1997). Offline trajectories: Calculation and accuracy (No. 44) [Software]. *Dept. of Meteorol., Univ. of Reading, U.K.: U.K. Univ. Global Atmos. Modelling Prog*. Retrieved from https://www.met.reading.ac.uk/~swrmethn/ROTRAJ/

Methven, J., Evans, M., Simmonds, P., & Spain, G. (2001). Estimating relationships between air mass origin and chemical composition. *Journal of Geophysical Research*, *106*(D5), 5005–5019. https://doi.org/10.1029/2000jd900694

Nicholson, S. (2016). The Turkana low-level jet: Mean climatology and association with regional aridity. *International Journal of Climatology*, *36*(6), 2598–2614. https://doi.org/10.1002/joc.4515

Peake, D., Dacre, H., Methven, J., & Coceal, O. (2014). Meteorological factors controlling low-level continental pollutant outflow across a coast. *Atmospheric Chemistry and Physics*, *14*(23), 13295–13312. https://doi.org/10.5194/acp-14-13295-2014

Poveda, G., Jaramillo, L., & Vallejo, L. (2014). Seasonal precipitation patterns along pathways of South American low-level jets and aerial rivers. *Water Resources Research*, *50*(1), 98–118. https://doi.org/10.1002/2013wr014087

Press, W., Teukolsky, S., Vetterling, W., & Flannery, B. (2003). *Numerical recipes: The art of scientific computing* (3rd ed.). Cambridge University Press.

Riddle, E., & Cook, K. (2008). Abrupt rainfall transitions over the Greater Horn of Africa: Observations and regional model simulations. *Journal of Geophysical Research*, *113*, D15109. https://doi.org/10.1029/2007jd009202

Rodwell, M., & Hoskins, B. (1995). A model of the Asian Summer Monsoon Part II: Cross-equatorial flow and PV behavior. *Journal of the Atmospheric Sciences*, *9*, 1341–1356. https://doi.org/10.1175/1520-0469(1995)052<1341:amotas>2.0.co;2

Schmitt, R., Bogden, P., & Dorman, C. (1989). Evaporation minus precipitation and density fluxes for the North Atlantic. *Journal of Physical Oceanography*, *19*(9), 1208–1221. https://doi.org/10.1175/1520-0485(1989)019<1208:empadf>2.0.co;2

Schmittner, A., Silva, T., Fraedrich, K., Kirk, E., & Lunkeit, E. (2011). Effects of mountains and ice sheets on global ocean circulation. *Journal of Climate*, *24*(11), 2814–2829. https://doi.org/10.1175/2010jcli3982.1

Silverman, B. (1986). *Density estimation for statistics and data analysis*. Chapman and Hall.

Simmons, A., & Burridge, D. (1981). An energy and angular-momentum conserving vertical finite-difference scheme and hybrid vertical coordinates. *Monthly Weather Review*, *109*(4), 758–766. https://doi.org/10.1175/1520-0493(1981)109<0758:aeaamc>2.0.co;2

Singh, H., Donohoe, A., Bitz, C., Nusbaumer, J., & Noone, D. (2016). Greater moisture transport distances with warming amplify interbasin salinity contrasts. *Geophysical Research Letters*, *43*(16), 8677–8684. https://doi.org/10.1002/2016gl069796

Sinha, B., Blaker, A., Hirschi, J.-M., Bonham, S., Brand, M., Josey, S., et al. (2012). Mountain ranges favour vigorous Atlantic meridional overturning. *Geophysical Research Letters*, *39*(2), L02705. https://doi.org/10.1029/2011gl050485

Stohl, A., & James, P. (2005). A Lagrangian analysis of the atmospheric branch of the global water cycle. Part II: Moisture transports between Earth's ocean basins and river catchments. *Journal of Hydrometeorology*, *6*, 961–984. https://doi.org/10.1175/jhm470.1

Stojanovic, M., Nieto, R., Liberato, M., Sorì, R., Vázquez, M., & Gimeno, L. (2021). Tracking the origins of moisture over Vietnam: The role of moisture sources and atmospheric drivers on seasonal hydroclimatic conditions. *International Journal of Climatology*, *41*(13), 5843–5861. https://doi.org/10.1002/joc.7156

Trenberth, K. (1998). Atmospheric moisture residence times and cycling: Implications for rainfall rates and climate change. *Climatic Change*, *39*(4), 667–694. https://doi.org/10.1023/a:1005319109110

Trenberth, K., Fasullo, J., & Mackaro, J. (2011). Atmospheric moisture transports from ocean to land and global energy flows in reanalyses. *Journal of Climate*, *24*(18), 4907–4924. https://doi.org/10.1175/2011jcli4171.1

van der Ent, R., & Savenije, H. (2013). Oceanic sources of continental precipitation and the correlation with sea surface temperature. *Water Resources Research*, *49*(7), 3993–4004. https://doi.org/10.1002/wrcr.20296

van der Ent, R., & Tuinenburg, O. (2017). The residence time of water in the atmosphere revisited. *Hydrology and Earth System Sciences*, *21*(2), 779–790. https://doi.org/10.5194/hess-21-779-2017

Vazquez, M., Nieto, R., Drumond, A., & Gimeno, L. (2016). Moisture transport into the Arctic: Source-receptor relationships and the roles of atmospheric circulation and evaporation. *Journal of Geophysical Research: Atmospheres*, *121*(22), 13493–13509. https://doi.org/10.1002/2016jd025400

Viste, E., & Sorteberg, A. (2011). Moisture transport into the Ethiopian highlands. *International Journal of Climatology*, *33*(1), 249–263. https://doi.org/10.1002/joc.3409

Volonté, A., Turner, A., & Menon, A. (2019). Airmass analysis of the processes driving the progression of the Indian Summer Monsoon. *Quarterly Journal of the Royal Meteorological Society*, *146*(731), 2949–2980. https://doi.org/10.1002/qj.3700

von Engeln, A., & Teixeira, J. (2013). A planetary boundary layer height climatology derived from ECMWF reanalysis data. *Journal of Climate*, *26*(17), 6575–6590. https://doi.org/10.1175/jcli-d-12-00385.1

Wainwright, C., Marsham, J., Keane, R., Rowell, D., Finney, D., Black, E., & Allan, R. (2019). 'Eastern African Paradox' rainfall decline due to shorter not less intense Long Rains. *npj Climate and Atmospheric Science*, *2*(34), 34. https://doi.org/10.1038/s41612-019-0091-7

Wang, C., & Enfield, D. (2001). The tropical Western Hemisphere warm pool. *Geophysical Research Letters*, *28*(8), 1635–1638. https://doi.org/10.1029/2000gl011763

Wang, C., Lee, S.-K., & Enfield, D. (2007). Impact of the Atlantic warm pool on the summer climate of the Western Hemisphere. *Journal of Climate*, *20*, 5021–5040. https://doi.org/10.1175/jcli4304.1

Wang, C., Zhang, L., & Lee, S.-K. (2013). Response of freshwater flux and sea surface salinity to variability of the Atlantic warm pool. *Journal of Climate*, *26*(4), 1249–1267. https://doi.org/10.1175/jcli-d-12-00284.1

Wei, H.-H., & Bordoni, S. (2016). On the role of the African topography in the South Asian Monsoon. *Journal of the Atmospheric Sciences*, *73*(8), 3197–3212. https://doi.org/10.1175/jas-d-15-0182.1

Whyte, F., Taylor, M., Stephenson, T., & Campbell, J. (2008). Features of the Caribbean low level jet. *International Journal of Climatology*, *28*(1), 119–128. https://doi.org/10.1002/joc.1510

Wills, R., & Schneider, T. (2015). Stationary eddies and the zonal asymmetry of net precipitation and ocean freshwater forcing. *Journal of Climate*, *28*(13), 5115–5133. https://doi.org/10.1175/jcli-d-14-00573.1

Xu, H., Xie, S.-S., Wang, Y., & Small, R. (2005). Effects of Central American mountains on the eastern Pacific winter ITCZ and moisture transport. *Journal of Climate*, *18*, 3856–3873. https://doi.org/10.1175/jcli3497.1

Yang, J.-C., Zhang, Y., Richter, I., & Lin, X. (2021). Interannual variability of tropical Atlantic-to-Pacific moisture transport linked to ENSO, Atlantic Niño, and the freshwater budget in the Northwestern Tropical Atlantic. *Journal of Climate*, *34*, 4625–4641.

Zaucker, F., & Broecker, W. (1992). The influence of atmospheric moisture transport on the fresh water balance of the Atlantic drainage basin: General circulation model simulations and observations. *Journal of Geophysical Research*, *97*(D3), 2765–2773. https://doi.org/10.1029/91jd01699